Reaction rates for the *s*-process neutron source ^{22}Ne + α

R. Longland,[1,2,3] C. Iliadis,[2,3] and A. I. Karakas[4]

[1]*Departament de Física i Enginyeria Nuclear, EUETIB, Universitat Politècnica de Catalunya, 08036 Barcelona, Spain*

[2]*Department of Physics and Astronomy, University of North Carolina at Chapel Hill, Chapel Hill, North Carolina 27599, USA*

[3]*Triangle Universities Nuclear Laboratory, Durham, North Carolina 27708, USA*

[4]*Research School of Astronomy & Astrophysics, Mount Stromlo Observatory, Weston Creek, ACT 2611, Australia*

(Received 14 May 2012; published 25 June 2012; corrected 29 June 2012)

The ^{22}Ne$(\alpha,n)^{25}$Mg reaction is an important source of neutrons for the *s*-process. In massive stars responsible for the weak component of the *s*-process, ^{22}Ne$(\alpha,n)^{25}$Mg is the dominant source of neutrons, both during core helium burning and in carbon-shell burning. For the main *s*-process component produced in asymptotic giant branch (AGB) stars, the ^{13}C$(\alpha,n)^{16}$O reaction is the dominant source of neutrons operating during the interpulse period, with the ^{22}Ne + α source affecting mainly the *s*-process branchings during a thermal pulse. Rate uncertainties in the competing ^{22}Ne$(\alpha,n)^{25}$Mg and ^{22}Ne$(\alpha,\gamma)^{26}$Mg reactions result in large variations of *s*-process nucleosynthesis. Here, we present up-to-date and statistically rigorous ^{22}Ne + α reaction rates using recent experimental results and Monte Carlo sampling. Our new rates are used in postprocessing nucleosynthesis calculations both for massive stars and AGB stars. We demonstrate that the nucleosynthesis uncertainties arising from the new rates are dramatically reduced in comparison to previously published results, but several ambiguities in the present data must still be addressed. Recommendations for further study to resolve these issues are provided.

DOI: 10.1103/PhysRevC.85.065809 PACS number(s): 26.20.Kn, 26.20.Fj, 25.55.−e, 24.30.−v

I. INTRODUCTION

The *s*-process is responsible for creating about half of the elements heavier than iron that are observed in the solar system [1]. This process involves the slow capture of neutrons (slower than the average β-decay rate of unstable nuclei) onto seed material, and hence nucleosynthesis follows the nuclear valley of stability. By considering the solar system abundances of *s*-only nuclei (that is, nuclei that can only be produced in the *s*-process) it can be shown that there are two key components of the *s*-process: the "main" component and the "weak" component [2]. The main component produces *s*-nuclei with masses of $A > 90$, while the weak component enriches the *s*-nuclei abundances at $A \lesssim 90$.

The main component of the *s*-process arises from neutron captures during He burning in $M \leqslant 4M_{\odot}$ asymptotic giant branch (AGB) stars. (For a detailed discussion of nuclear burning in AGB stars see Refs. [3,4].) In low-mass ($0.8M_{\odot}$ to $4M_{\odot}$) AGB stars of solar metalicity, most neutrons are released through the ^{13}C$(\alpha,n)^{16}$O reaction during the interpulse period, while the ^{22}Ne$(\alpha,n)^{25}$Mg reaction produces an additional burst of neutrons during thermal pulses. This burst of neutrons affects mainly the branchings in the *s*-process path. In intermediate-mass AGB stars ($M > 4M_{\odot}$), where the temperatures are expected to be higher, the ^{22}Ne$(\alpha,n)^{25}$Mg reaction is thought to be the main source of neutrons and could explain the enhancement of rubidium seen in some metal-poor AGB stars [5–9]. In addition to *s*-process elements, the ^{22}Ne$(\alpha,n)^{25}$Mg and ^{22}Ne$(\alpha,\gamma)^{26}$Mg rates influence the relative production of ^{25}Mg and ^{26}Mg, whose abundance ratios can be measured to high precision in circumstellar ("presolar") dust grains. Magnesium is also one of the few elements for which the isotopic ratios (^{25}Mg/^{24}Mg and ^{26}Mg/^{24}Mg) can be derived from stellar spectra (for example, Refs. [10,11]). However, Karakas *et al.* [12] showed that with their estimated ^{22}Ne$(\alpha,n)^{25}$Mg and ^{22}Ne$(\alpha,\gamma)^{26}$Mg reaction rate uncertainties, the relative abundances of ^{25}Mg and ^{26}Mg predicted by their stellar models can vary by up to 60%.

The weak component of the *s*-process arises from nuclear burning in massive stars. The core temperature in these stars (typically with $M \gtrsim 11M_{\odot}$) becomes high enough during He burning for the ^{22}Ne$(\alpha,n)^{25}$Mg reaction to produce a high flux of neutrons shortly before the helium fuel is exhausted. Any remaining ^{22}Ne releases a second flux of neutrons during convective carbon-shell burning. The *s*-process yield in these stars is therefore sensitive to the temperature at which the ^{22}Ne$(\alpha,n)^{25}$Mg reaction starts to produce an appreciable flux of neutrons. The *et al.* [13] showed that the *s*-process during the core-He-burning stage in massive stars depends strongly on both the ^{22}Ne + α and the ^{16}O$(n,\gamma)^{17}$O reaction rates. They also found that not only are the overall uncertainties in the rates important but so is the temperature dependence of the rates.

The ^{22}Ne + α reactions also affect nucleosynthesis in other astrophysical environments. During type II supernova explosions, two γ-ray emitting radionuclides, ^{26}Al and ^{60}Fe, are ejected, and their abundance ratio provides a sensitive constraint on stellar models (see [14] and references therein). The species ^{60}Fe is mainly produced in massive stars by neutron captures during convective carbon-shell burning (e.g., Ref. [15]). Its abundance, therefore, depends strongly on the ^{22}Ne + α rates. The ^{22}Ne + α rates also play a role in type Ia supernovae. Throughout the "simmering" stage, roughly 1000 years prior to the explosion, Piro and Bildsten *et al.* [16] suggested that neutrons released by the ^{22}Ne$(\alpha,n)^{25}$Mg reaction affect the carbon abundance, thus altering the amount of ^{56}Ni produced (i.e., the peak luminosity) in the explosion. Timmes *et al.* [17] also found that during the explosion, neutronization by the ^{22}Ne$(\alpha,n)^{25}$Mg reaction affects the electron mole fraction, Y_e, thus influencing the nature of the explosion.

In this work we will evaluate new reaction rates for ^{22}Ne + α. Compared to previous results [12,18,19] our new rates are significantly improved because (i) we incorporate all the recently obtained data on resonance fluorescence absorption, α-particle transfer, etc., and (ii) we employ a sophisticated (Monte Carlo) method to estimate the rates and associated uncertainties. We have recently presented new ^{22}Ne + α rates in Ref. [20] but did not give a detailed account of their calculation. Since the latter results were published, we found, and could account for, a number of inconsistencies in data previously reported in the literature. In addition, new data from Ref. [21] became available, which have been included in the present work. Thus the rates presented here supersede our earlier results [20].

The paper will be organized as follows: in Sec. II a detailed discussion of the Monte Carlo method used to calculate reaction rates is discussed. This method is described in detail elsewhere [22] but will be summarized to show its applicability to the specific cases of the ^{22}Ne + α reactions. The ^{22}Ne + α rate calculations and comparisons with the literature will be presented in Sec. III. The reaction rates will then be used to present new nucleosynthesis yields along with their uncertainties in Sec. VI. Conclusions will be presented in Sec. VII.

II. REACTION RATE FORMALISM

A. Thermonuclear reaction rates

The reaction rate per particle pair in a plasma of temperature T is given by

$$\langle \sigma v \rangle = \sqrt{\frac{8}{\pi \mu}} \frac{1}{(kT)^{3/2}} \int_0^\infty E \sigma(E) e^{-E/kT} dE, \quad (1)$$

where μ is the reduced mass of the reacting particles, $\mu = M_0 M_1/(M_0 + M_1)$; M_i denotes the masses of the particles; k is the Boltzmann constant; E is the center-of-mass energy of the reacting particles; and $\sigma(E)$ is the reaction cross section at energy, E.

The strategy for determining reaction rates from Eq. (1) depends on the nature of the cross section. In many cases the cross section can be separated into nonresonant and resonant parts. Reactions such as ^{22}Ne + α proceed through the compound nucleus ^{26}Mg at relatively high excitation energy ($Q_{\alpha\gamma}$ = 10614.787(33) keV [23]) and are frequently dominated by resonant capture. The nonresonant part of the cross section will, therefore, be neglected in the following discussion. The reader is referred to Refs. [22,24] for more details.

The resonant part of the cross section can be represented in one of two ways: (i) by narrow resonances, whose partial widths can be assumed to be approximately constant over the resonance width ("narrow resonances"), and (ii) by wide resonances, for which the resonant cross section must be integrated numerically to account for the energy dependence of the partial widths involved. The reaction rates per particle pair for single, isolated narrow and wide resonances, respectively, are given by

$$\langle \sigma v \rangle = \left(\frac{2\pi}{\mu kT} \right)^{3/2} \hbar^2 \omega\gamma e^{-E_r/kT} \quad (2)$$

and

$$\langle \sigma v \rangle = \frac{\sqrt{2\pi}\hbar^2}{(\mu kT)^{3/2}} \omega \int_0^\infty \frac{\Gamma_a(E)\Gamma_b(E)}{(E - E_r)^2 + \Gamma(E)^2/4} e^{-E/kT} dE, \quad (3)$$

where the resonance strength $\omega\gamma$ is defined by

$$\omega\gamma = \omega \Gamma_a \Gamma_b / \Gamma; \quad (4)$$

E_r is the resonance energy; $\Gamma_a(E)$, $\Gamma_b(E)$, and $\Gamma(E)$ are the energy-dependent entrance channel (particle) partial width, exit channel partial width, and total width, respectively; and ω, the statistical spin factor, is defined by $\omega = (2J + 1)/(2J_0 + 1)(2J_1 + 1)$, where J and J_i are the resonance and particle spins, respectively. The particle partial width, Γ_c, can be written as the product of an energy-independent reduced width, γ_c^2, and an energy-dependent penetration factor, $P_c(E)$, as

$$\Gamma_c = 2 P_c(E) \gamma_c^2. \quad (5)$$

For the present case of ^{22}Ne + α, the entrance channel (α-particle) reduced width, γ_α^2, is related to the α-particle spectroscopic factor, S_α, by

$$\gamma_\alpha^2 = \frac{\hbar^2}{\mu a^2} \theta_\alpha^2 \quad (6)$$

$$= \frac{\hbar^2}{2\mu a} S_\alpha \phi^2(a), \quad (7)$$

where $\phi(a)$ is the single-particle radial wave function at the channel radius, a (see, for example, [25,26]). The constant $\hbar^2/(\mu a^2)$ is the Wigner limit (in the notation of Lane and Thomas [27]). It can be regarded as an upper limit, according to the sum rules in the dispersion theory of nuclear reactions; i.e., $\theta_\alpha^2 \leqslant 1$. Note that it is frequently assumed that $\theta^2 = S$, which must be regarded as a crude approximation only. For example, in the case of ^{17}O levels it was shown in Ref. [28] that S_α exceeds θ_α^2 by at most a factor of 2. We will return to these issues in Sec. III C.

The above relationships are useful since they allow for an estimation of the important α-particle partial widths from spectroscopic factors obtained in α-particle transfer reactions, as will be discussed later. It is important to note that the value of S_α depends on the parameters of the nuclear potentials assumed in the transfer data analysis. Similarly, the value of γ_α^2 depends on the channel radius. However, if, throughout the analysis, consistent values of these parameters (such as a) are used, their impact on the value of Γ_α will be strongly reduced.

B. Monte Carlo reaction rates

The equations outlined in Sec. II A provide the tools for calculating thermonuclear reaction rates given available estimates for the cross-section parameters (E_r, $\omega\gamma$, etc.). A problem arises, however, when statistically rigorous uncertainties of the reaction rates are desired. What is usually presented in

the literature are recommended rates, together with upper and lower "limits," but the reported values are not derived from a suitable probability density function. Therefore, the reported values have no rigorous statistical meaning. An attempt to construct a method for analytical uncertainty propagation of reaction rates was made by Thompson & Iliadis [29]. However, their method is applicable only in special cases, when the uncertainties in resonance parameters are relatively small. Thompson & Iliadis [29] were also unable to treat the uncertainty propagation for reaction rates that need to be integrated or for rates that include upper limits on some parameters. For these reasons, a Monte Carlo method is used in the present study to calculate statistically meaningful reaction rates.

The general strategy of Monte Carlo uncertainty[1] propagation is as follows: (i) randomly sample from the probability density distribution of each input parameter; (ii) calculate the reaction rates for each randomly sampled parameter set on a grid of temperatures (using the same set at each temperature); (iii) repeat steps (i) and (ii) many times (on the order of 5000). Steps (i)–(iii) will result in a distribution at each temperature grid point that can be interpreted as the probability density function of the reaction rate. Extraction of uncertainties from this distribution will be discussed later. While input parameter sampling is being performed, care must be taken to consider correlations in parameters. For example, particle partial widths depend on the penetration factor, which is an energy-dependent quantity. The individual energy samples must, therefore, be propagated consistently through resonance energy and partial width estimation in order to fully account for the correlation of these quantities. The code RATESMC [22] was used to perform the Monte Carlo sampling and to analyze the probability densities of the total reaction rates.

In order to apply Monte Carlo sampling to calculate reaction rate uncertainties, sampling distributions must be chosen for each input parameter. Once a reaction rate (output) distribution has been computed, an appropriate mathematical description must be found to present the result in a convenient manner. Statistical distributions important for reaction rate calculations are described in detail in Refs. [22,30] and are summarized briefly below.

Uncertainties of resonance energies are determined by the *sum* of different contributions. In this case, the central limit theorem of statistics predicts that resonance energies are Gaussian distributed. Note that there is a finite probability of calculating a negative resonance energy and that this choice of probability density naturally accounts for the inclusion of subthreshold resonances in the above formalism. A resonance strength or a partial width, on the other hand, is experimentally derived from the *product* of measured input quantities (e.g., count rates, stopping powers, detection efficiencies, etc.). In such a case the central limit theorem predicts that resonance strengths or partial widths are log-normally distributed.

[1]Throughout this work, care is taken to refer to the terms *uncertainty* and *error* correctly. The term *error* refers to a quantity that is believed to be incorrect, whereas *uncertainty* refers to the spread estimate of a parameter.

The log-normal probability density for a resonance strength or a partial width is given by

$$f(x) = \frac{1}{\sigma\sqrt{2\pi}}\frac{1}{x}e^{-(\ln x-\mu)^2/(2\sigma^2)}, \tag{8}$$

with the log-normal parameters μ and σ representing the mean and standard deviation of $\ln x$. These quantities are related to the expectation value, $E[x]$, and variance, $V[x]$, by

$$\mu = \ln(E[x]) - \frac{1}{2}\ln\left(1+\frac{V[x]}{E[x]^2}\right),$$
$$\sigma = \sqrt{\ln\left(1+\frac{V[x]}{E[x]^2}\right)}. \tag{9}$$

The quantities $\ln(E[x])$ and $\sqrt{V[x]}$ can be associated with the central value and uncertainty, respectively, that are commonly reported. Note that a log-normal distribution is only defined for positive values of x. This feature is crucial because it removes the finite probability of sampling unphysical, negative values when Gaussian uncertainties are used. This is especially true for partial width measurements, which frequently have uncertainties in the 20%–50% range. Note, also, that a 50% Gaussian uncertainty results in a 3% probability of the partial width having a value below zero.

The important problem of estimating reaction rates when only upper limits of resonance strengths or partial widths are available will now be discussed. The standard practice in nuclear astrophysics (see, for example, [18,31]) is to adopt 10% resonance strength upper limit values for the calculation of the *recommended* total rates. "Lower limits" or "upper limits" of rates are then derived by completely excluding or by adopting the full upper limit, respectively, for all resonance strengths. This procedure is questionable for two reasons. First, without further knowledge, it is implicitly assumed that the probability density for the resonance strength is a uniform distribution extending from zero to the upper limit value. The implication is that the *mean value* of the resonance strength amounts to half of its upper limit value. This conclusion contradicts fundamental nuclear physics, as will be explained below. Second, the derived "upper limit" and "lower limit" on the total reaction rate are usually interpreted as sharp boundaries. This conclusion is also unphysical, as will be explained below.

The strength of a resonance depends on particle partial widths, which can be expressed in terms of reduced widths, γ^2, or, alternatively, spectroscopic factors, S (see Sec. II A). These quantities depend on the overlap between the incoming channel $(a + A)$ and the compound nucleus final state, which in turn depends on a nuclear matrix element. If the nuclear matrix element has contributions from many different parts of configuration space, and if the signs of these contributions are random, then the central limit theorem predicts that the probability density of the transition amplitude will tend toward a Gaussian distribution centered at zero. The probability density of the reduced width, representing the *square* of the amplitude, is then given by a chi-squared distribution with one degree of freedom. These arguments were first presented by Porter & Thomas [32] and this probability density is

also known as the Porter-Thomas distribution. For a particle channel it can be written as

$$f(x) = \frac{c}{\sqrt{\theta^2}} e^{-\theta^2/(2\hat{\theta}^2)}, \tag{10}$$

where c is a normalization constant, θ^2 is the dimensionless reduced width, and $\hat{\theta}^2$ is the local mean value of the dimensionless reduced width. The distribution implies that the reduced width for a given nucleus and set of quantum numbers varies by several orders of magnitude, with a higher probability the smaller the value of the reduced width. The Porter-Thomas distribution emerges naturally from the Gaussian orthogonal ensemble of random matrix theory and is well established experimentally (see Ref. [33] for a recent review).[2]

The above discussion provides a physically sound method for randomly sampling reduced widths (or spectroscopic factors) if only an upper limit value is available. Furthermore, in the present work we assume a sharp truncation of the Porter-Thomas distribution at the upper limit value for the dimensionless reduced width, θ^2_{ul}; that is, we randomly sample over the probability density

$$f(\theta) = \begin{cases} \frac{c}{\sqrt{\theta^2}} e^{-\theta^2/(2\hat{\theta}^2)} & \text{if} \quad \theta^2 \leqslant \theta^2_{ul}, \\ 0 & \text{if} \quad \theta^2 > \theta^2_{ul}. \end{cases} \tag{11}$$

Once dimensionless reduced widths are obtained from sampling according to Eq. (11), samples of particle partial widths can be found from Eq. (5). Subsequently, samples of resonance strengths can be determined from Eq. (4).

In order to utilize Eq. (11) for Monte Carlo sampling of α-particle partial widths, the mean value of the dimensionless reduced width, $\hat{\theta}^2_\alpha$, must be known. To this end we considered 360 α-particle reduced widths in the $A = 20$–40 mass region (see [36] and references therein). The distribution is shown in Fig. 1 as a black histogram. Binning and fitting the data to Eq. (10) (solid line) results in a best-fit value of $\hat{\theta}^2_\alpha = 0.010$, which we adopt in the present work. It is important to recall the above arguments: the distribution of reduced widths for a given nucleus, given orbital angular momentum, given channel spin, etc. is expected to follow a Porter-Thomas distribution. However, because of the relatively small sample size of 360 values, we were compelled to fit the entire set by disregarding differences in nuclear mass number and orbital angular momentum. For this reason, our derived mean value of 0.010 must be regarded as preliminary. More reliable estimates of $\hat{\theta}^2_\alpha$ have to await the analysis of a significantly larger data set of α-particle reduced widths when it becomes available in the future.

[2]Recently, in a high-precision study of neutron partial widths in platinum ($A = 192, 194$) by Koehler *et al.* [34] and a reanalysis of the Nuclear Data Ensemble ($A = 64$–238) in Ref. [35] it has been claimed that the data are not well described by a χ^2 distribution with one degree of freedom ($\nu = 1$, i.e., a Porter-Thomas distribution). These authors find, depending on the data set under consideration, values between $\nu = 0.5$ and $\nu = 1.2$. These new results are controversial and more studies are needed before the issue can be settled. It is not clear at present whether this controversy has any implications for the compound nucleus ^{26}Mg.

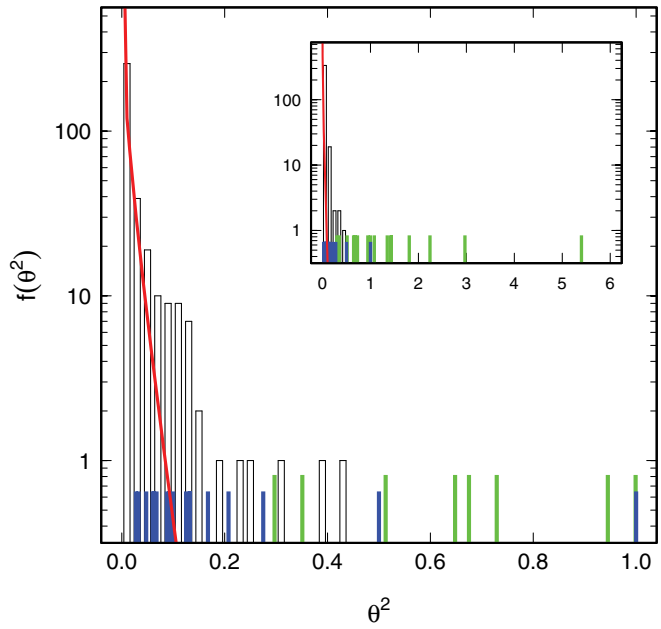

FIG. 1. (Color online) Dimensionless reduced α-particle widths of unbound states from Ref. [36] and references therein (see also [22]). Also plotted is the Porter-Thomas distribution that best fits these data at small values. It is apparent from the figure that states with large α-particle spectroscopic factors are not represented by the Porter-Thomas distribution. These levels most likely have an α-particle cluster structure and would be populated preferentially in transfer measurements, such as the (^{6}Li, d) measurements of Refs. [44,56]. Also shown in green and blue are the normalized spectroscopic factors measured in Ref. [44]. The values normalized using the $E_r^{\rm lab} = 1434$ keV resonance are shown in blue, while those normalized to the $E_r^{\rm lab} = 831$ keV resonance are shown in green. Clearly, the normalizations are vastly different, and the spectroscopic factors obtained using the $E_r^{\rm lab} = 831$ keV resonance as a normalization reference appear to be too high, as shown in the figure inset, which displays the same information but on an expanded scale. See text for more detail.

From the arguments presented above it should also be clear that the Porter-Thomas distribution is not expected to represent the reduced width of all nuclear levels, particularly if the amplitude is dominated by a few large contributions of configuration space. The most important example for the latter situation are α-cluster states, which are expected to have relatively large reduced widths. Indeed, the large reduced width values in Fig. 1 that are not described by the Porter-Thomas distribution (solid line) originate most likely from α-cluster states. Clearly, the nuclear structure of a level in question must be considered carefully. For this reason, results from α-particle transfer studies are very important. It can be argued that these measurements populate preferentially α-cluster states, with large reduced widths (or spectroscopic factors), while levels not populated in α transfer have small reduced widths and, therefore, are more likely statistical in nature (i.e., described by a Porter-Thomas distribution). This issue will become important in later sections.

Once a random sampling of all input parameters has been performed, an ensemble of reaction rates is obtained. From its

probability density one can extract descriptive statistics (mean, median, variance, etc.). For the recommended reaction rate, we adopt the median value. The median is a useful statistic because exactly half of the calculated rates lie above this value and half below. Note that we do not use the mean value because it is strongly affected by outliers in the reaction rate distribution. The low and high reaction rates are obtained by assuming a 68% coverage probability. There are several methods for obtaining these coverage probabilities, such as finding the coverage that minimizes the range of the uncertainties or one that is centered on the median. In the present work, the 16th to 84th percentiles of the cumulative reaction rate distribution are used. We emphasize an important point regarding reaction rate uncertainties: contrary to previous work, our "low" and "high" rates do not represent sharp boundaries (i.e., a probability density of zero outside the boundaries). As with any other continuous probability density function, these values depend on the assumed coverage probability, i.e., assuming a larger coverage will result in a larger uncertainty of the total reaction rate (which is further illustrated in Figs. 4 and 5). The important point here is that the Monte Carlo sampling results in "low" and "high" rates for which the coverage probability can be quantified precisely.

Although low, high, and median rates are useful quantities, they do not necessarily contain all the information on the rate probability density. For application of a reaction rate to nucleosynthesis calculations, therefore, it is useful to approximate the rate probability density by a simple analytical approximation. It was shown in [22] that in most (but not all) cases the reaction rate probability density is well approximated by a log-normal distribution [Eq. (8)]. The log-normal parameters μ and σ can be found from the sampled total rates at each temperature according to

$$\mu = E[\ln(y)], \quad \sigma^2 = V[\ln(y)], \tag{12}$$

where $E[\ln(y)]$ and $V[\ln(y)]$ denote the expectation value and variance of the natural logarithm of the total rate, y, respectively. A useful measure of the applicability of a log-normal approximation to the actual sampled distribution is provided by the Anderson-Darling (A-D) statistic,[3] which is calculated from

$$t_{AD} = -n - \sum_{i=1}^{n} \frac{2i-1}{n} \{\ln F(y_i) + \ln[1 - F(y_{n+1-i})]\}, \tag{13}$$

where n is the number of samples, y_i are the sampled reaction rates at a given temperature (arranged in ascending order), and F is the cumulative distribution of a standard normal function (i.e., a Gaussian centered at zero). An A-D value greater than unity indicates a deviation from a log-normal distribution. However, it was found by Longland *et al.* [22] that the rate distribution does not *visibly* deviate from log-normal until A-D exceeds $t_{AD} \approx 30$. The A-D statistic is presented in Tables VI and VII along with the reaction rates at each temperature in order to provide a reference to the reader.

[3]The Anderson-Darling statistic [37] is more useful than a χ^2 statistic because it does not require binning of the data. The latter usually results in a loss of information.

C. Extrapolation of experimental reaction rates to higher temperatures

Experimental rates usually need to be extrapolated to high temperatures with the aid of theoretical models because resonances are only measured up to some finite energy, $E_{\rm max}^{\rm exp}$. If the effective stellar burning energy window [38] extends above this energy, the rate calculated using the procedure outlined above will become inaccurate. Statistical nuclear reaction models must, therefore, be used to extrapolate the experimental rates beyond this temperature. The method used here is described in detail in Ref. [38]. It uses the following strategy: (i) an effective thermonuclear energy range (ETER) is defined using the 8th, 50th, and 92nd percentiles of the cumulative distribution of fractional reaction rates (i.e., the relative contribution of single resonances at temperature T divided by the total reaction rate at T); (ii) the temperature, $T_{\rm match}$, beyond which the total rate must be extrapolated is estimated from

$$E(T_{\rm match}) + \Delta E(T_{\rm match}) = E_{\rm max}^{\rm exp}, \tag{14}$$

where $\Delta E(T_{\rm match})$ is the width of the ETER calculated from the 8th and 92nd rate percentiles. We adopt the Hauser-Feshbach rates of Ref. [39] for temperatures beyond $T_{\rm match}$, normalized to the experimental rate at $T_{\rm match}$.

III. THE ^{22}Ne + α REACTIONS

A. General aspects

The ^{22}Ne$(\alpha,n)^{25}$Mg [$Q_{\alpha n} = -478.296(89)$ keV] and ^{22}Ne$(\alpha,\gamma)^{26}$Mg [$Q_{\alpha\gamma} = 10614.787(33)$ keV] reactions are both important in s-process neutron production. While the ^{22}Ne$(\alpha,n)^{25}$Mg reaction produces neutrons, the ^{22}Ne$(\alpha,\gamma)^{26}$Mg reaction also influences the neutron flux by directly competing for available α particles. The rates of both reactions will therefore be presented here. The center-of-mass energy region of interest to the s-process amounts to $E_{\rm cm} = 600 \pm 300$ keV, corresponding to excitation energies of $E_x = 10900$–11500 keV in the ^{26}Mg compound nucleus. Note that only states of "natural" parity (i.e., 0^+, 1^-, 2^+, etc.) can be populated via ^{22}Ne + α (because both target and projectile have spin-parities of 0^+).

Since the early 1980s, several direct measurements were performed of both reactions close to the energy region of interest [19,40–44]. All of these measurements, with the exception of those of Ref. [44], were made using gas targets at the Institut für Strahlenphysik in Stuttgart, Germany (e.g., [45]). The lowest energy resonance measured in those works is located at $E_r^{\rm lab} \approx 830$ keV, near the high-energy end of the astrophysically important region. The structure of the ^{26}Mg compound nucleus near the α-particle and neutron thresholds has been investigated previously via neutron capture [46,47], scattering [48–50], photoexcitation [51–53], transfer [44,54–56], and photoneutron measurements [57]. In

TABLE I. New information relevant to the ^{22}Ne + α reaction rates that has become available since the NACRE compilation was published [18].

Reference	Reaction studied	Comments
Jaeger *et al.* [19]	^{22}Ne$(\alpha,n)^{25}$Mg	Resonances between $E_r^{\rm lab} = 570$ keV and $E_r^{\rm lab} = 1450$ keV
Koehler [60]	$^{\rm nat}$Mg(n,γ)	E_x, J^π, Γ_γ, Γ_n for states corresponding to $E_r^{\rm lab} = 570$ keV to $E_r^{\rm lab} = 1000$ keV
Ugalde *et al.* [56]	^{22}Ne$(^6$Li$,d)^{26}$Mg	J^π and S_α for two states below neutron threshold
Longland *et al.* [59]	^{26}Mg$(\vec{\gamma},\gamma')^{26}$Mg	E_x and J^π for four resonances corresponding to $E_r^{\rm lab} = 38$ keV to $E_r^{\rm lab} = 636$ keV
deBoer *et al.* [21]	^{26}Mg$(\vec{\gamma},\gamma')^{26}$Mg	Γ_γ for four resonances corresponding to $E_r^{\rm lab} = 38$ keV to $E_r^{\rm lab} = 636$ keV

particular, the latter study observed the strong population of a ^{26}Mg level near $E_x = 11\,150$ keV, with presumed quantum numbers of $J^\pi = 1^-$, corresponding to an expected low-energy resonance at $E_{\rm cm} = 450$ keV. It was believed to have been observed by Drotleff *et al.* [42] and Harms *et al.* [41] at $E_r^{\rm lab} = 630$ keV, but the presumed signal was later shown to be caused by background from the ^{11}B$(\alpha,n)^{14}$N reaction. Nevertheless, the anticipated contribution from this low-energy resonance has sensitively influenced all past estimates of ^{22}Ne + α reaction rates. For example, it was shown by The *et al.* [58] that it has a strong impact on *s*-process nucleosynthesis in massive stars. However, recent ^{26}Mg$(\vec{\gamma},\ \gamma)^{26}$Mg studies by Longland *et al.* [59] demonstrated unambiguously that this particular level has unnatural parity ($J^\pi = 1^+$) and, therefore, cannot be populated via α-particle capture on ^{22}Ne.

Studies that provide new experimental information relevant to ^{22}Ne + α, obtained after the NACRE compilation was published [18], are summarized in Table I. The goal of the following discussion is to consider all the available experimental information for states in ^{26}Mg of interest to *s*-process nucleosynthesis and to assign these levels to corresponding resonances in both ^{22}Ne$(\alpha,\gamma)^{26}$Mg and ^{22}Ne$(\alpha,n)^{25}$Mg. This allows for an estimation of the partial and total resonance widths, resulting in more accurate ^{22}Ne + α reaction rates. A number of levels in ^{26}Mg near the α-particle and neutron thresholds have unknown spin-parities and partial widths. These levels have been disregarded in all previous reaction rate estimates. Since it is not known at present if any of these are natural parity states and, therefore, may be populated in ^{22}Ne + α, they cannot be easily included in a Monte Carlo reaction rate analysis at present. Thus, our strategy is as follows: We will first derive ^{22}Ne + α Monte Carlo rates by excluding these levels of unknown spin-parities. Subsequently, we will investigate their impact on the total reaction rates *under the extreme assumption that all of these levels possess natural parity*. As will be seen below, future measurements of these states are highly desirable. Throughout the following discussion, energies are presented in the center-of-mass frame unless otherwise stated.

B. Resonance strengths

Directly measured resonance strengths in the ^{22}Ne$(\alpha,\gamma)^{26}$Mg reaction in the energy range of $E_r^{\rm lab} = 830$–2040 keV are adopted from Ref. [40]. Direct measurements of resonances in the ^{22}Ne$(\alpha,n)^{25}$Mg reaction at energies of $E_r^{\rm lab} = 830$–2040 keV are reported in Refs. [19,40,41,43,44]. Note, however, that the ^{22}Ne$(\alpha,n)^{25}$Mg resonance strengths from the different measurements disagree by up to a factor of 5 (i.e., a deviation well outside the quoted uncertainties). Clearly, adopting a simple weighted average value would not account for the unknown systematic bias present in the data. To alleviate this problem, we adopt the method of Ref. [61], previously applied to account for unknown systematic uncertainties in neutron-lifetime measurements. This method follows a procedure for characterizing unknown systematic uncertainties similar to that presented in Ref. [62]. It assumes that all the reported strength values of a given resonance have the same, unknown, systematic error, σ_u, which can be summed in quadrature with the reported uncertainties. Hence for each reported uncertainty of data set i, σ_i, an inflated uncertainty, σ_i', is obtained via

$$\sigma_i' = \sqrt{\sigma_u^2 + \sigma_i^2}. \tag{15}$$

From the inflated uncertainties, the weighted average of the resonance strengths, $\omega\gamma_i$, is obtained in the usual manner,

$$\overline{\omega\gamma} = \frac{\sum_i \omega\gamma_i/\sigma_i'^2}{\sum_i 1/\sigma_i'^2}, \qquad \overline{\sigma} = \sqrt{\frac{1}{\sum_i 1/\sigma_i'^2}}. \tag{16}$$

The unknown value of σ_u is adjusted numerically until the reduced chi-squared value, χ^2/ν, becomes equal to unity:

$$\frac{\chi^2}{\nu} = \frac{1}{n-1}\sum_i \frac{(\omega\gamma_i - \overline{\omega\gamma})^2}{\sigma_i'^2}, \tag{17}$$

where ν is the degree of freedom (i.e., $\nu = n - 1$, with n equal to the number of measurements).

Application of this method has two consequences compared to calculating the weighted average of the reported resonance strength values: (i) the uncertainty of the resonance strength, $\overline{\sigma}$, will be larger, reflecting the fact that the systematic shift in the data is of unknown nature, and (ii) strength values with small reported uncertainties will carry less weight. Consider as an example the lowest lying observed resonance in the ^{22}Ne$(\alpha,n)^{25}$Mg reaction, located at $E_r^{\rm lab} = 831$ keV. The measurements reported in Refs. [19,41,43,44] yield for the resonance strength a (standard) weighted average of $\omega\gamma = 1.2(1) \times 10^{-4}$ eV, with $\chi^2/\nu = 2.9$, indicating poor agreement between the individual measurements. On the other hand, the inflated weighted average value is $\omega\gamma = 1.4(3) \times 10^{-4}$ eV. We applied the inflated weighted average method to all resonances in the energy region $E_r^{\rm lab} = 830$–1495 keV. Above this energy

range, we used the (standard) weighted average because the different data sets are in considerably better agreement.

From the measured ^{22}Ne$(\alpha,n)^{25}$Mg and ^{22}Ne$(\alpha,\gamma)^{26}$Mg strengths of a given resonance, the neutron and α-particle partial widths can be found if the γ-ray partial width can be estimated. This information allows for integrating the resonance cross section numerically, according to Eq. (3), which is more reliable than adopting the narrow-resonance approximation, Eq. (2). Because of Coulomb barrier penetrability arguments, the neutron width is expected to dominate the total width of the resonances important for s-process nucleosynthesis (i.e., $\Gamma_n \approx \Gamma$). Thus, in most (but not all) cases, the neutron width exceeds the α-particle width for a given state substantially and we can use the following approximations to determine the α-particle width from measured resonance strengths. For the ^{22}Ne$(\alpha,\gamma)^{26}$Mg reaction, the α-particle partial width can be found by assuming a reasonable average value for the γ-ray partial width of $\Gamma_\gamma \approx 3$ eV [60]. We investigated the effect of this choice on the reaction rates and the exact average value of Γ_γ was found to be relatively unimportant. The α-particle partial width can then be found (for $\Gamma_n \approx \Gamma$) from

$$\omega\gamma_{\alpha\gamma} = \omega\frac{\Gamma_\alpha\Gamma_\gamma}{\Gamma_\alpha+\Gamma_\gamma+\Gamma_n}, \qquad \Gamma_\alpha = \frac{\omega\gamma_{\alpha\gamma}}{\omega}\frac{\Gamma}{3\text{ eV}}. \quad (18)$$

For the ^{22}Ne$(\alpha,n)^{25}$Mg reaction, the α-particle partial width can be calculated from

$$\omega\gamma_{\alpha n} = \omega\frac{\Gamma_\alpha\Gamma_n}{\Gamma_\alpha+\Gamma_\gamma+\Gamma_n}, \qquad \Gamma_\alpha = \frac{\omega\gamma_{\alpha n}}{\omega}. \quad (19)$$

C. Spectroscopic factors

Alpha-particle spectroscopic factors for levels near the α-particle and neutron thresholds in ^{26}Mg have been obtained from ^{22}Ne$(^6\text{Li},d)^{26}$Mg transfer studies by Refs. [44,56]. The spectroscopic factors derived from the $(^6\text{Li},d)$ transfer data are important because they allow for an estimate of the α-particle partial width, Γ_α, of $^{22}\text{Ne}+\alpha$ resonances via Eqs. (6), (7), and (5).

Numerous studies have shown that α-transfer measurements are very useful for measuring relative spectroscopic factors, but they are not sufficiently accurate for predicting absolute values. For this reason, the measured spectroscopic factors are frequently scaled relative to resonances with well-known partial widths. (Note that this is an approximation equivalent to assuming that $\theta^2 = S$ in Sec. II.) For example, Giesen *et al.* [44] scaled their spectroscopic factors relative to the $E_r^{\text{lab}} = 831$ keV ($J^\pi = 2^+$) resonance in ^{22}Ne$(\alpha,n)^{25}$Mg. Our best value for the (α,n) resonance strength is $\omega\gamma_{\alpha n} = 1.4(3)\times10^{-4}$ eV (see Table IV). Since for this low-energy resonance it can be safely assumed that $\Gamma \approx \Gamma_n$, a spectroscopic factor of $S_\alpha^{(\alpha,n)} = 0.98$ is obtained from Eqs. (4) and (5). Surprisingly, this value is a factor of 27 larger than the transfer value extracted by Ref. [44], $S_\alpha^{(^6\text{Li},d)} = 0.037$. Renormalization of all measured $(^6\text{Li},d)$ spectroscopic factors to the (α,n) spectroscopic factor of the $E_r^{\text{lab}} = 831$ keV resonance results in the values shown in green in Fig. 1. It is certainly remarkable that all levels observed by Ref. [44] should have dimensionless reduced α-particle widths far larger in value than the Porter-Thomas prediction. Additionally, several of these levels exhibit dimensionless reduced widths near or exceeding the Wigner limit, even if one accounts for the difference between S_α and θ_α^2 (Sec. II A).

However, there is no compelling reason why the $E_r^{\text{lab}} = 831$ keV resonance should be singled out for the normalization procedure, other than it being the lowest lying observed resonance. For example, one may consider another well-known resonance, located at $E_r^{\text{lab}} = 1434$ keV ($J^\pi = 2^+$). From its measured ^{22}Ne$(\alpha,n)^{25}$Mg resonance strength, an α-particle spectroscopic factor of $S_\alpha^{(\alpha,n)} = 0.27$ is obtained. The α-particle transfer value for the corresponding levels, measured by Ref. [44], amounts to $S_\alpha^{(^6\text{Li},d)} = 0.11$. These two values differ by a factor of 2.5, and thus they are much closer in agreement than the results for the $E_r^{\text{lab}} = 831$ keV resonance. Normalization of all measured relative $(^6\text{Li},d)$ spectroscopic factors to the (α,n) spectroscopic factor of the $E_r^{\text{lab}} = 1434$ keV resonance results in the values shown in blue in Fig. 1. It is evident that these normalized values are in far better agreement with the Porter-Thomas distribution than the results obtained when scaling spectroscopic factors relative to the $E_r^{\text{lab}} = 831$ keV resonance. In addition, by using the $E_r^{\text{lab}} = 1434$ keV resonance normalization, all of the resulting dimensionless reduced widths now have values less than the Wigner limit, making them more believable. Since we feel it is more reasonable to scale the $(^6\text{Li},d)$ spectroscopic factors using the $E_r^{\text{lab}} = 1434$ keV resonance instead of the $E_r^{\text{lab}} = 831$ keV resonance, we adopt the reduced widths shown in blue in Fig. 1 for calculating the $^{22}\text{Ne}+\alpha$ rates. Note that the *relative* spectroscopic factors obtained by Ref. [44] have been used at face value by Refs. [12,60] in their reaction rate calculations. Clearly, this issue needs to be resolved in future work.

IV. INFORMATION ON SPECIFIC ^{26}Mg LEVELS

A. $E_x = 10\,693$ keV ($E_r^{\text{lab}} = 92$ keV; $J^\pi = 4^+$)

An excited state near this energy has been observed by Glatz *et al.* [54] at $E_x = 10\,695(2)$ keV, Giesen *et al.* [44] at $E_x = 10\,694(20)$ keV, and Moss [49] at $E_x = 10\,689(3)$ keV. A weighted average of these excitation energies is used in the present work. The $J^\pi = 4^+$ assignment was made by considering the decay scheme of this state as observed by Ref. [54] and that the state most likely has natural parity. The α-particle spectroscopic factor for this state from Ref. [44], after normalization, is $S_\alpha = 0.059$.

B. $E_x = 10\,806$ keV ($E_r^{\text{lab}} = 226$ keV; $J^\pi = 1^-$)

This state was seen previously in ^{22}Ne$(^6\text{Li},d)^{26}$Mg measurements by Ugalde *et al.* [56] at $E_x = 10\,808(20)$ keV and in ^{25}Mg$(n_t,\gamma)^{26}$Mg measurements (thermal neutron capture) by Walkiewicz *et al.* [63] at $E_x = 10\,805.9(4)$ keV. A recent experiment assigned a spin-parity of $J^\pi = 1^-$ [59]. The adopted excitation energy is the weighted average of these results. The α-particle spectroscopic factor from Ref. [56], after normalization, amounts to $S_\alpha = 0.048$.

C. $E_x = 10\,943$ keV ($E_r^{\rm lab} = 388$ keV; $J^\pi = 5^-$–7^-)

An excited state at this energy has been observed by Glatz *et al.* [54]. The observed decay scheme restricts the quantum numbers, using the dipole-or-$E2$ rule of Ref. [64], to $J^\pi = (5^\pm$–$7^-)$. A ^{22}Ne(^{6}Li, d)^{26}Mg transfer measurement populated a state at $E_x = 10\,953(25)$ keV, but Glatz *et al.* did not obtain the quantum numbers other than to report that it most likely had natural parity [56]. The combined quantum number assignment is therefore $J^\pi = (5^-$–$7^-)$. This state is treated here as part of a doublet with the $E_x = 10\,949$ keV state. Note that in the reaction rate calculations of Karakas *et al.* [12], this state was incorrectly assigned spin-parity values of $J^\pi = 2^+, 3^-$.

D. $E_x = 10\,949$ keV ($E_r^{\rm lab} = 395$ keV; $J^\pi = 1^-$)

This state has been observed previously in ^{26}Mg(p, p')^{26}Mg measurements by Moss [49] at $E_x = 10\,950(3)$ keV. The (p, p') measurements suggest a $J^\pi = 1^-$ assignment, which agrees with the ^{26}Mg($\vec{\gamma}$, γ)^{26}Mg result of Longland *et al.* [59]. It is unclear whether Ugalde *et al.* [56] observed this state or the one at $E_x = 10\,943$ keV. Therefore, in the present analysis, the normalized spectroscopic factor of $S = 7 \times 10^{-3}$ reported in Ref. [56] is treated as an upper limit for both states at $E_x = 10\,943$ keV and $E_x = 10\,949$ keV.

E. $E_x = 11\,112$ keV ($E_r^{\rm lab} = 587$ keV; $J^\pi = 2^+$)

The state is located above the neutron threshold. It has been observed previously in a ^{25}Mg(n, γ)^{26}Mg experiment [47,60] and was assigned a spin-parity of $J^\pi = 2^+$.

F. $E_x = 11\,154$ keV ($E_r^{\rm lab} = 637$ keV; $J^\pi = 1^+$)

A state at this energy has been observed by Fagg [48], Weigmann *et al.* [47], Crawley *et al.* [52], Yasue *et al.* [55], Koehler [60], Tamii *et al.* [50], and Schwengner *et al.* [53]. Additionally, an excited state at this energy was strongly populated by the photoneutron experiment of Berman *et al.* [57], who predicted a $J^\pi = 1^-$ assignment. As a result of this prediction, a resonance corresponding to this energy has been sought in several studies [19,41–44,56]. Of these studies, a presumed resonance was reported in Refs. [41,42], but this was later proven to be caused by beam-induced background [43]. Recently, however, a ^{26}Mg($\vec{\gamma}$, γ)^{26}Mg experiment [59] showed unambiguously that the spin-parity of this state amounts to $J^\pi = 1^+$ and, therefore, cannot contribute to the ^{22}Ne + α reactions rates. A more detailed discussion of this state is presented in Sec. III A.

G. $E_x = 11\,163$–$11\,326$ keV ($E_r^{\rm lab} = 648$–840 keV)

Excitation energies were taken as weighted averages of values from Moss [49], Glatz *et al.* [54], and Koehler [60]. Quantum numbers and neutron and γ-ray partial widths were all adopted from Ref. [60]. Since no α-particle partial widths have been measured for these states, upper limits were either derived from the data presented by Ref. [40] or adopted from the maximum theoretically allowed values, depending on which was smaller.

H. $E_x = 11\,318$ keV ($E_r^{\rm lab} = 831$ keV; $J^\pi = 2^+$)

Koehler [60] argued that this state cannot correspond to both the resonance observed by Jaeger *et al.* [19] at $E_r = 832(2)$ keV in ^{22}Ne(α, n)^{25}Mg and that found by Wolke *et al.* [40] at $E_r^{\rm lab} = 828(5)$ keV in ^{22}Ne(α, γ)^{26}Mg, because the implied value of $\Gamma_\gamma = 76$ eV would be far larger than the average γ-ray partial width ($\Gamma_\gamma = 3$ eV) in this energy range. However, this conclusion is questionable given the large uncertainty, $\Gamma_\gamma = 76(53)$ eV, when the γ-ray partial width is derived from the measured values of $\omega\gamma_{\alpha\gamma}$, $\omega\gamma_{\alpha n}$, and Γ. Clearly, the deviation from the average in this energy range amounts to only 1.4σ.

Since it cannot be decided at present whether or not the (α, n) and (α, γ) resonances correspond to the same ^{26}Mg level, the partial widths cannot be derived unambiguously from the measured resonance strengths and total width. Thus we assumed that the (α, n) and (α, γ) resonances are "narrow"; i.e., we employed Eq. (2) instead of Eq. (3) in our rate calculations. The strength reported by Ref. [40] is used for the ^{22}Ne(α, γ)^{26}Mg resonance, while the inflated weighted average (see Sec. III B) is adopted for the ^{22}Ne(α, n)^{25}Mg resonance, resulting in a strength of $\omega\gamma_{(\alpha,n)} = 1.4(3) \times 10^{-4}$ eV.

I. $E_x = 11\,328$–$11\,425$ keV ($E_r^{\rm lab} = 843$–957 keV)

Excitation energies, quantum numbers, and neutron and γ-ray widths for these levels are adopted from Refs. [47] and [60]. No α-particle widths have been measured for these states, and thus upper limits have been adopted from either the data presented by Refs. [19,40] or from the maximum theoretically allowed values, depending on which was smaller.

J. $E_x > 11\,441$ keV ($E_r^{\rm lab} > 976$ keV)

Resonances corresponding to excited states above $E_x = 11\,441$ keV have been measured directly [19,40–44]. In order to take the widths of wide resonances into account, the neutron and γ-ray partial widths (and quantum numbers) measured by Refs. [47,60] have been used when available. The inflated weighted average method (see Sec. III B) is used to combine the different ^{22}Ne(α, n)^{25}Mg strengths for resonances below $E_r^{\rm lab} = 1434$ keV, while standard weighted averages are used above this energy. Since the ^{22}Ne(α, γ)^{26}Mg resonances measured in Ref. [40] cannot be assigned unambiguously to corresponding ^{22}Ne(α, n)^{25}Mg resonances, all of these resonances were treated as independent and narrow. The quantum numbers of ^{22}Ne(α, n)^{25}Mg resonances located above $E_r^{\rm lab} = 1530$ keV are adopted from Ref. [40] when not available otherwise.

V. REACTION RATES FOR ^{22}Ne + α

The resonance properties used to calculate the rates for both the ^{22}Ne(α, γ)^{26}Mg and the ^{22}Ne(α, n)^{25}Mg reactions are presented in Tables II–V. For more detailed information on level properties, see Ref. [30]. Separate tables are used to

TABLE II. Resonances of ^{22}Ne$(\alpha,\gamma)^{26}$Mg with known α-particle partial widths or resonance strengths. Total widths are from Ref. [40] for resonances above $E_r^{\rm lab} = 1533$ keV. For lower lying resonances, total widths are adopted from Ref. [19] and Ref. [60]. Ambiguous spin-parities (i.e., those not based on strong arguments) are placed in parentheses, according to the guidelines in Ref. [64]. The last column, labeled "Int" indicates those resonances for which sufficient information is available in order to integrate their reaction rate contribution numerically, according to Eq. (3).

				Partial widths (eV)				
E_x (keV)	$E_r^{\rm lab}$ (keV)	J^π [c]	$\omega\gamma$ (eV)	Γ_α	Γ_γ [a]	Γ_n	Γ	Int
10693	93 (2)	4^+	—	$3.5(18)\times10^{-46}$	3.0 (15)	—	3.0 (15)	
11315	828 (5)	2^+	$3.6(4)\times10^{-5}$	—	—	—	—	
11441	976.39 (23)	4^+	—	$4.3(11)\times10^{-6}$ [b]	3.0 (15)	$1.47\ (8)\times10^3$	$1.47\ (8)\times10^3$	✓
11465	1005.23 (25)	5^-	—	$5.0(15)\times10^{-6}$ [b]	3.0 (15)	$6.55\ (9)\times10^3$	$6.55\ (9)\times10^3$	✓
11508	1055.9 (11)	1^-	—	$1.2(2)\times10^{-4}$ [b]	3.0 (15)	$1.27\ (25)\times10^4$	$1.27\ (25)\times10^4$	✓
11526	1075.5 (18)	1^-	—	$4.3(11)\times10^{-4}$ [b]	3.0 (15)	$1.8\ (9)\times10^3$	$1.8\ (9)\times10^3$	✓
11630	1202.3 (17)	1^-	—	$2.4(5)\times10^{-3}$ [b]	3.0 (15)	$1.35\ (17)\times10^4$	$1.35\ (17)\times10^4$	✓
11748	1345 (7)	1^-	—	$2.0(3)\times10^{-2}$ [b]	3.0 (15)	$6.4\ (9)\times10^4$	$6.4\ (9)\times10^4$	✓
11787	1386 (3)	1^-	—	$8(3)\times10^{-3}$ [b]	3.0 (15)	$2.45\ (24)\times10^4$	$2.45\ (24)\times10^4$	✓
11828	1433.7 (12)	2^+	$2.5(3)\times10^{-4}$	$1.8(10)\times10^{-1}$	3.0 (15)	$1.10\ (25)\times10^3$	$1.10\ (25)\times10^3$	✓
11895	1513 (5)	1^-	$2.0(2)\times10^{-3}$	—	—	—	<3000	
11912	1533 (3)	$1^-, 2^+$	$3.4(4)\times10^{-3}$	$1.9(8)\times10^{+0}$	3.0 (15)	$5\ (2)\times10^3$	$5\ (2)\times10^3$	✓
11953	1582 (3)	$2^+, 3^-, 4^+$	$3.4(4)\times10^{-3}$	$3.2(17)\times10^{-1}$	3.0 (15)	$2\ (1)\times10^3$	$2\ (1)\times10^3$	✓
12051	1698 (3)	$2^+, 3^-$	$6.0(7)\times10^{-3}$	$1.1(3)\times10^{-1}$	3.0 (15)	$4\ (1)\times10^3$	$4\ (1)\times10^3$	✓
12140	1802 (3)	1^-	$1.0(2)\times10^{-3}$	$1.7(5)\times10^{+0}$	3.0 (15)	$15\ (2)\times10^3$	$15\ (2)\times10^3$	✓
12184	1855 (8)	(0^+)	$1.1(2)\times10^{-3}$	$1.21(29)\times10^{+1}$	3.0 (15)	$33\ (5)\times10^3$	$33\ (5)\times10^3$	✓
12273	1960 (8)	(0^+)	$8.9(1)\times10^{-3}$	$2.2(4)\times10^{+2}$	3.0 (15)	$73\ (9)\times10^3$	$73\ (9)\times10^3$	✓
12343	2043 (5)	0^+	$5.4(7)\times10^{-2}$	$6.3(12)\times10^{+2}$	3.0 (15)	$35\ (5)\times10^3$	$35\ (5)\times10^3$	✓

[a] Average value from Ref. [60].
[b] From ^{22}Ne$(\alpha,n)^{25}$Mg measurements [see Eq. (19)].
[c] A detailed discussion on quantum number assignments can be found in Sec. III B.

list resonances with measured partial widths and those which possess only an upper limit for the α-particle width but have known neutron and γ-ray widths.

The matching temperature, $T_{\rm match}$ (see Sec. II C), for both the ^{22}Ne$(\alpha,\gamma)^{26}$Mg and ^{22}Ne$(\alpha,n)^{25}$Mg reactions, beyond which the rates are estimated by normalizing Hauser-Feshbach predictions to experimental rates, amounts to $T = 1.33$ GK, i.e., well above the temperatures relevant for the s-process during He burning ($T = 0.01$–0.3 GK).

Monte Carlo reaction rates for the ^{22}Ne$(\alpha,\gamma)^{26}$Mg and ^{22}Ne$(\alpha,n)^{25}$Mg reactions are presented in Tables VI and VII, respectively. The median, low, and high rates are shown alongside the log-normal parameters and the Anderson-Darling statistic described in Sec. II B. The Monte Carlo reaction rate probability density functions are displayed in Figs. 2 and 3 as red histograms. The solid black lines indicate the log-normal approximation, calculated with the log-normal parameters, μ and σ, listed in columns 5, 6, 10, and 11 of Tables VI and VII.

In order to emphasize that our low and high rates, obtained for a coverage probability of 68% (see Sec. II B), do not represent sharp boundaries, we show the (α,γ) and (α,n) reaction rates, normalized to the respective recommended (median) values, as color contours in Figs. 4 and 5. The thick and thin solid lines represent coverage probabilities of 68% and 95%, respectively. The three dashed lines show the previously reported rates (Angulo *et al.* [18] for ^{22}Ne$(\alpha,\gamma)^{26}$Mg and Jaeger *et al.* [19] for ^{22}Ne$(\alpha,n)^{25}$Mg), normalized to our recommended rate. Our calculations of the relative resonance contributions to the total (α,γ) and (α,n) reaction rates show that, at temperatures most relevant to the s-process, resonances including and below the $E_r^{\rm lab} = 831$ keV resonance are the most important. Future experimental efforts should, therefore, be concentrated on studying resonances in the excitation energy region near the neutron threshold.

For the ^{22}Ne$(\alpha,\gamma)^{26}$Mg reaction, the present rates deviate significantly from the results of Ref. [18], by factors of 2–100. The differences are caused by (i) a different treatment of partial widths; in Ref. [18] the rates were found from numerical integration by assuming upper limit values ($\Gamma = 4$–10 keV) for the total widths, whereas in the present work total widths have been adopted from measured values; (ii) our improved treatment of upper limits for reduced α-particle widths (i.e., sampling over a Porter-Thomas distribution; see Sec. II B); and (iii) the fact that new nuclear data became available since 1999 (see Table I). The combined effect of these improvements results in a factor of 5 reduction in reaction rate uncertainties in the He-burning temperature region.

As already noted in Sec. III A, a number of excited states near the α-particle and neutron thresholds in ^{26}Mg have been observed in additional inelastic proton scattering experiments [49,50,52]. However, their spins and parities have not been determined. In particular, it is not known at present whether these levels possess natural parity and thereby may be populated in the ^{22}Ne $+\,\alpha$ reactions. In order to investigate the maximum impact of these states with unknown J^π values on the ^{22}Ne$(\alpha,\gamma)^{26}$Mg reaction rate, we performed a test by

TABLE III. Properties of unobserved resonances in ^{22}Ne$(\alpha,\gamma)^{26}$Mg . For these resonances, only upper limits of the resonance strength and/or the α-particle spectroscopic factor are available at present. The γ-ray and neutron partial widths are taken from the R-matrix fit of Ref. [60]. Quantum numbers for states below $E_x = 11\,163$ keV are discussed in Sec. IV. All other quantum numbers are adopted from Ref. [60]. When a range of quantum numbers is allowed, the upper limit of the α-particle width is calculated by assuming the lowest possible orbital angular momentum transfer. The upper limit α-particle spectroscopic factors adopted ($S_{\alpha,\mathrm{UL}}$) are also listed for completeness.

				Partial widths (eV)					
E_x (keV)	E_r^{lab} (keV)	J^π	$\omega\gamma_{\mathrm{UL}}$ (eV)	$S_{\alpha,\mathrm{UL}}$	$\Gamma_{\alpha,\mathrm{UL}}$	Γ_γ	Γ_n	Γ	Int
10806	225.9 (5)	1^-	—	4.8×10^{-2}	3.2×10^{-23}	0.72(18)	—	0.72(18)	
10943	388 (2)	$(5^- - 7^-)$	—	7×10^{-3}	1.5×10^{-19}	3.0(15)	—	3.0(15)	
10949	395.15 (18)	1^-	—	7×10^{-3}	2.9×10^{-15}	1.9(3)	—	1.9(3)	
11112	587.90 (10)	2^+	3.7×10^{-08}	1.00	7.7×10^{-09}	1.73(3)	2578(240)	2580(240)	✓
11163	647.93 (11)	2^+	4.3×10^{-07}	1.00	8.7×10^{-08}	4.56(29)	4640(100)	4650(100)	✓
11171	657.53 (19)	(2^+)	6.2×10^{-07}	1.00	1.3×10^{-07}	3.0(15)	1.44(16)	4.4(15)	
11183	671.70 (21)	(1^-)	1.0×10^{-06}	1.00	2.1×10^{-07}	3.0(15)	0.54(9)	3.5(15)	
11243	742.81 (12)	$2^{(-)}$	4.7×10^{-06}	0.44	9.5×10^{-07}	7.4(6)	4510(110)	4520(110)	✓
11274	779.32 (14)	$(2)^+$	4.9×10^{-06}	0.15	1.0×10^{-06}	3.2(4)	540(50)	540(50)	✓
11280	786.17 (13)	$4^{(-)}$	8.2×10^{-07}	1.00	9.2×10^{-08}	0.59(24)	1510(30)	1510(30)	✓
11286	792.90 (15)	1^-	5.0×10^{-06}	0.05	1.7×10^{-06}	0.8(5)	1260(100)	1260(100)	✓
11286	793.83 (14)	(2^+)	5.0×10^{-06}	0.11	1.0×10^{-06}	4.3(6)	12.8(6)	17.1(60)	✓
11289	797.10 (29)	(2^-)	5.1×10^{-06}	0.10	1.0×10^{-06}	3.0(15)	1.5(5)	4.5(16)	
11296	805.19 (16)	(3^-)	5.1×10^{-06}	0.39	7.4×10^{-07}	3.3(7)	8060(120)	8060(120)	✓
11311	822.6 (4)	(1^-)	5.2×10^{-06}	0.02	1.8×10^{-06}	3.0(15)	1.1(4)	4.1(16)	
11326	840.8 (6)	(1^-)	5.4×10^{-06}	0.01	1.8×10^{-06}	3.0(15)	0.6(3)	3.6(15)	
11328	843.24 (17)	1^-	5.4×10^{-06}	0.01	1.8×10^{-06}	3.6(5)	420(90)	420(90)	✓
11329	844.4 (6)	(1^-)	5.4×10^{-06}	0.01	1.8×10^{-06}	3.0(15)	2.8(10)	5.8(18)	
11337	853.6 (7)	(1^-)	5.4×10^{-06}	0.01	1.8×10^{-06}	3.0(15)	1.4(6)	4.4(18)	
11344	861.86 (18)	(2^+)	5.5×10^{-06}	0.02	1.1×10^{-06}	1.18(27)	150(40)	150(40)	✓
11345	862.91 (19)	$4^{(-)}$	5.5×10^{-06}	0.87	6.2×10^{-07}	1.8(4)	4130(190)	4130(190)	✓
11393	919.34 (19)	$5^{(+)}$	1.6×10^{-06}	1.00	1.5×10^{-07}	3.0(15)	290(19)	290(19)	✓

assuming that all of these levels possess natural parity and by adopting upper limit α-particle spectroscopic factors from that data of Refs. [44] and [56]. The results show that these states can increase the ^{22}Ne$(\alpha,\gamma)^{26}$Mg reaction rate by up to a factor of 30 at temperatures between $T_9 = 0.1$ and 0.2 GK.

For the ^{22}Ne$(\alpha,n)^{25}$Mg reaction there is better agreement between previous and new rates. The present rates are slightly higher (up to a factor of 2) than those calculated in Ref. [19]. The two main reasons for the difference are as follows: (i) we used inflated weighted averages of the reported resonance strengths from different measurements (see Sec. III B) and (ii) we excluded the contribution of a presumed $E_r^{\mathrm{lab}} = 630$ keV resonance, because the level at $E_x = 11\,154$ keV has been shown to possess unnatural parity [59].

We would like to emphasize that the observed (α,n) and (α,γ) resonances near $E_r^{\mathrm{lab}} = 830$ keV introduce another systematic uncertainty that we have not accounted for. Recall that we treated these two resonances as independent and narrow (Sec. IV). On the other hand, if they correspond to the same level in ^{26}Mg, the partial widths could be derived from the measured resonance strengths. In that case, the resonance turns out to be relatively broad, resulting in a significant contribution of the resonance tail to the total reaction rate. Tests show that the resulting reaction rates near $T \approx 0.3$ GK could increase by roughly a factor of 5.

The ratio of ^{22}Ne$(\alpha,n)^{25}$Mg to ^{22}Ne$(\alpha,\gamma)^{26}$Mg reaction rates is shown in Fig. 6. Note that these rates are not independent since, for example, the same values of α-particle partial widths enter in both rate calculations if an (α,γ) and (α,n) resonance corresponds to the same ^{26}Mg level. Thus the uncertainties shown in Fig. 6 are somewhat overestimated. Nevertheless, it is instructive to compare the present ratios, shown in black, to those from previous work [18,19], displayed in red. It can be seen that the present ratio is significantly larger than previous results and, consequently, we predict that more neutrons will be produced per captured α particle.

VI. ASTROPHYSICAL IMPLICATIONS

A. Models

In order to explore how the current ^{22}Ne $+\,\alpha$ reaction rates affect s-process nucleosynthesis, two kind of calculations are presented here. The first compares final abundance yields from postprocessing models upon changing the *recommended* ^{22}Ne $+\,\alpha$ reaction rates from previously published results to those presented in this paper. The second calculation estimates the variations in s-process nucleosynthesis arising from uncertainties in the present ^{22}Ne $+\,\alpha$ reaction rates. These can then be compared with abundance variations arising from the literature rates.

In order to take the uncertainties into account, three sets of calculations were performed: (i) recommended rates for both ^{22}Ne$(\alpha,n)^{25}$Mg and ^{22}Ne$(\alpha,\gamma)^{26}$Mg reactions, (ii) low ^{22}Ne$(\alpha,n)^{25}$Mg rate and high ^{22}Ne$(\alpha,\gamma)^{26}$Mg rate, and

TABLE IV. Resonances in ^{22}Ne$(\alpha,n)^{25}$Mg with known α-particle partial widths or resonance strengths. When a range of quantum numbers is present, the one used for calculating the reaction rates is presented in bold.

				Partial widths (eV)				
E_x(keV)	$E_r^{\rm lab}$ (keV)	J^π [a]	$\omega\gamma$ (eV)	Γ_α [b]	Γ_γ [c]	Γ_n [d]	Γ	Int
11318	830.8 (13)	2^+	$1.4(3)\times10^{-4}$	—	—	—	$2.5\ (17)\times10^{2}$	
11441	976.39 (23)	4^+	$3.9(10)\times10^{-5}$	$4.3(11)\times10^{-6}$	3.0 (15)	$1.47\ (8)\times10^{3}$	$1.47\ (8)\times10^{3}$	✓
11465	1005.23 (25)	5^-	$5.5(17)\times10^{-5}$	$5.0(15)\times10^{-6}$	3.0 (15)	$6.55\ (9)\times10^{3}$	$6.55\ (9)\times10^{3}$	✓
11508	1055.9 (11)	1^-	$3.5(6)\times10^{-4}$	$1.17(20)\times10^{-4}$	3.0 (15)	$1.27\ (25)\times10^{4}$	$1.27\ (25)\times10^{4}$	✓
11525	1075.5 (18)	1^-	$1.3(3)\times10^{-3}$	$4.3(11)\times10^{-4}$	3.0 (15)	$1.8\ (9)\times10^{3}$	$1.8\ (9)\times10^{3}$	✓
11632	1202.3 (17)	1^-	$7.1(15)\times10^{-3}$	$2.4(5)\times10^{-3}$	3.0 (15)	$1.35\ (17)\times10^{4}$	$1.35\ (17)\times10^{4}$	✓
11752	1345 (7)	1^-	$5.9(8)\times10^{-2}$	$2.0(3)\times10^{-2}$	3.0 (15)	$6.4\ (9)\times10^{4}$	$6.4\ (9)\times10^{4}$	✓
11788	1386 (3)	1^-	$2.5(9)\times10^{-2}$	$8(2)\times10^{-3}$	3.0 (15)	$2.45\ (24)\times10^{4}$	$2.45\ (24)\times10^{4}$	✓
11828	1433.7 (12)	2^+	$8.5(14)\times10^{-1}$	$1.7(3)\times10^{-1}$	3.0 (15)	$1.10\ (25)\times10^{3}$	$1.10\ (25)\times10^{3}$	✓
11863	1475 (3)	1^-	$5(3)\times10^{-2}$	$1.5(10)\times10^{-2}$	3.0 (15)	$2.45\ (34)\times10^{4}$	$2.45\ (34)\times10^{4}$	✓
11880	1495 (3)	1^-	$1.9(19)\times10^{-1}$	—	—	—	—	
11890	1507.9 (16)	1^-	$4.1(4)\times10^{-1}$	—	—	—	—	
11910	1530.9 (15)	$\mathbf{1}^-, 2^+$	$1.40(10)\times10^{+0}$	—	—	—	—	
11951	1579.4 (15)	$2^+, \mathbf{3}^-, 4^+$	$1.60(13)\times10^{+0}$	—	—	—	—	
12050	1696.7 (15)	$\mathbf{2}^+, 3^-$	$4.7(3)\times10^{+0}$	—	—	—	—	
12111	1768.2 (18)	1^-	$7.1(6)\times10^{-1}$	—	—	—	—	
12141	1803.5 (15)	1^-	$2.4(2)\times10^{+0}$	—	—	—	—	
12184	1855 (6)	(0^+)	$9.0(11)\times10^{-1}$	—	—	—	—	
12270	1956 (6)	(0^+)	$2.1(2)\times10^{+1}$	—	—	—	—	
12345	2044.8 (18)	0^+	$1.57(10)\times10^{+2}$	—	—	—	—	
12435	2152 (10)	1^-	$2.8(7)\times10^{+1}$	—	—	—	—	
12551	2289 (15)	1^-	$1.2(5)\times10^{+2}$	—	—	—	—	

[a] A detailed discussion of quantum number assignment can be found in the text.
[b] Calculated using Eq. (19).
[c] Average value from Ref. [60].
[d] Assuming Γ is dominated by Γ_n (see Sec. III A).

TABLE V. Properties of unobserved resonances in ^{22}Ne$(\alpha,n)^{25}$Mg . For these resonances, only upper limits of the resonance strength and/or the α-particle spectroscopic factor can be derived. Quantum numbers and γ-ray and neutron partial widths are taken from the R-matrix fit of Ref. [60]. Resonance energies represent a weighted average of values adopted from Refs. [47,49,54,60].

				Partial widths (eV)					
E_x (keV)	$E_r^{\rm lab}$ (keV)	J^π	$\omega\gamma_{\rm UL}$ (eV)	S_α	$\Gamma_{\alpha,\rm UL}$	Γ_n	Γ_γ	Γ	Int
11112	587.90 (10)	2^+	5.8×10^{-8}	1.00	7.7×10^{-9}	2580(240)	1.73(3)	2580(240)	✓
11163	647.93 (11)	2^+	1.9×10^{-7}	0.44	3.8×10^{-8}	4640(100)	4.56(29)	4650(100)	✓
11171	657.53 (19)	(2^+)	7.5×10^{-8}	0.12	1.5×10^{-8}	1.44(16)	3.0(15)	4.4(15)	
11183	671.70 (21)	(1^-)	7.7×10^{-5}	1.00	2.1×10^{-7}	0.54(9)	3.0(15)	3.5(15)	
11243	742.81 (12)	$2^{(-)}$	1.2×10^{-7}	0.01	2.4×10^{-8}	4510(110)	7.4(6)	4520(110)	✓
11274	779.33 (14)	$(2)^+$	1.1×10^{-7}	3.5×10^{-3}	2.2×10^{-8}	540(50)	3.2(4)	540(50)	✓
11280	786.17 (13)	$4^{(-)}$	1.3×10^{-7}	0.16	1.4×10^{-8}	1510(30)	0.59(24)	1510(30)	✓
11286	792.90 (15)	1^-	7.7×10^{-8}	7.3×10^{-4}	2.6×10^{-8}	1260(100)	0.8(5)	1260(100)	✓
11286	793.83 (14)	(2^+)	7.7×10^{-8}	1.6×10^{-3}	1.5×10^{-8}	13(6)	4.3(6)	17(6)	✓
11289	797.10 (29)	(2^-)	7.7×10^{-8}	1.5×10^{-3}	1.5×10^{-8}	1.5(5)	3.0(15)	4.5(16)	
11296	805.19 (16)	(3^-)	1.0×10^{-7}	7.7×10^{-3}	1.4×10^{-8}	8060(120)	3.3(7)	8060(120)	✓
11311	822.6 (4)	(1^-)	1.6×10^{-8}	7.5×10^{-5}	5.8×10^{-9}	1.1(4)	3.0(15)	4.1(16)	
11326	840.8 (6)	(1^-)	1.2×10^{-7}	3.6×10^{-4}	4.5×10^{-8}	0.6(3)	3.0(15)	3.6(15)	
11328	843.24 (17)	1^-	5.0×10^{-7}	1.3×10^{-3}	1.7×10^{-7}	420(90)	3.6(5)	430(90)	✓
11329	844.4 (6)	(1^-)	1.2×10^{-7}	3.3×10^{-4}	4.5×10^{-8}	2.8(10)	3.0(15)	5.8(18)	
11337	853.6 (7)	(1^-)	1.3×10^{-7}	2.7×10^{-4}	4.6×10^{-8}	1.4(6)	3.0(15)	4.4(18)	
11344	861.86 (18)	(2^+)	2.0×10^{-7}	7.2×10^{-4}	4.0×10^{-8}	150(40)	1.18(27)	150(40)	✓
11345	862.91 (19)	$4^{(-)}$	4.2×10^{-8}	7.2×10^{-4}	5.1×10^{-9}	4130(190)	1.8(4)	4130(190)	✓
11393	919.34 (19)	$5^{(+)}$	3.7×10^{-8}	2.4×10^{-2}	3.7×10^{-9}	290(19)	3.0(15)	293(19)	✓

TABLE VI. Monte Carlo reaction rates for the ^{22}Ne$(\alpha,\gamma)^{26}$Mg reaction. Shown are the low, median, and high rates, corresponding to the 16th, 50th, and 84th percentiles of the Monte Carlo probability density distributions. Also shown are the parameters (μ and σ) of the log-normal approximation to the actual Monte Carlo probability density. See Ref. [22] for details. The rate values shown in parentheses indicate the temperatures ($T > T_{\rm match} = 1.33$ GK) for which Hauser-Feshbach rates, normalized to experimental results, are adopted (see Sec. II C).

T (GK)	Low rate	Median rate	High rate	log-normal μ	log-normal σ
0.010	1.05×10^{-77}	2.14×10^{-77}	4.52×10^{-77}	$-1.765 \times 10^{+02}$	7.42×10^{-01}
0.011	3.99×10^{-74}	7.28×10^{-74}	1.34×10^{-73}	$-1.684 \times 10^{+02}$	6.15×10^{-01}
0.012	3.69×10^{-71}	6.34×10^{-71}	1.07×10^{-70}	$-1.617 \times 10^{+02}$	5.34×10^{-01}
0.013	1.15×10^{-68}	1.90×10^{-68}	3.09×10^{-68}	$-1.559 \times 10^{+02}$	4.92×10^{-01}
0.014	1.55×10^{-66}	2.52×10^{-66}	4.04×10^{-66}	$-1.511 \times 10^{+02}$	4.80×10^{-01}
0.015	1.06×10^{-64}	1.73×10^{-64}	2.79×10^{-64}	$-1.468 \times 10^{+02}$	4.90×10^{-01}
0.016	4.11×10^{-63}	6.96×10^{-63}	1.14×10^{-62}	$-1.431 \times 10^{+02}$	5.13×10^{-01}
0.018	1.80×10^{-60}	3.26×10^{-60}	5.63×10^{-60}	$-1.370 \times 10^{+02}$	5.75×10^{-01}
0.020	2.24×10^{-58}	4.34×10^{-58}	8.04×10^{-58}	$-1.321 \times 10^{+02}$	6.43×10^{-01}
0.025	1.54×10^{-54}	3.14×10^{-54}	6.30×10^{-54}	$-1.232 \times 10^{+02}$	7.13×10^{-01}
0.030	2.82×10^{-50}	3.35×10^{-49}	1.30×10^{-48}	$-1.121 \times 10^{+02}$	$1.87 \times 10^{+00}$
0.040	1.81×10^{-42}	2.31×10^{-41}	8.91×10^{-41}	$-9.413 \times 10^{+01}$	$2.14 \times 10^{+00}$
0.050	8.51×10^{-38}	1.08×10^{-36}	4.17×10^{-36}	$-8.338 \times 10^{+01}$	$2.15 \times 10^{+00}$
0.060	1.05×10^{-34}	1.34×10^{-33}	5.14×10^{-33}	$-7.624 \times 10^{+01}$	$2.08 \times 10^{+00}$
0.070	1.95×10^{-32}	2.12×10^{-31}	8.04×10^{-31}	$-7.104 \times 10^{+01}$	$1.79 \times 10^{+00}$
0.080	2.76×10^{-30}	1.14×10^{-29}	3.67×10^{-29}	$-6.679 \times 10^{+01}$	$1.33 \times 10^{+00}$
0.090	1.76×10^{-28}	6.30×10^{-28}	1.35×10^{-27}	$-6.289 \times 10^{+01}$	$1.15 \times 10^{+00}$
0.100	4.79×10^{-27}	2.28×10^{-26}	6.55×10^{-26}	$-5.931 \times 10^{+01}$	$1.35 \times 10^{+00}$
0.110	8.17×10^{-26}	5.95×10^{-25}	1.86×10^{-24}	$-5.616 \times 10^{+01}$	$1.55 \times 10^{+00}$
0.120	1.11×10^{-24}	9.63×10^{-24}	3.07×10^{-23}	$-5.343 \times 10^{+01}$	$1.64 \times 10^{+00}$
0.130	1.23×10^{-23}	1.03×10^{-22}	3.28×10^{-22}	$-5.102 \times 10^{+01}$	$1.57 \times 10^{+00}$
0.140	1.38×10^{-22}	8.23×10^{-22}	2.50×10^{-21}	$-4.883 \times 10^{+01}$	$1.36 \times 10^{+00}$
0.150	1.53×10^{-21}	5.57×10^{-21}	1.51×10^{-20}	$-4.679 \times 10^{+01}$	$1.10 \times 10^{+00}$
0.160	1.41×10^{-20}	3.79×10^{-20}	8.10×10^{-20}	$-4.484 \times 10^{+01}$	8.63×10^{-01}
0.180	8.05×10^{-19}	1.54×10^{-18}	2.84×10^{-18}	$-4.102 \times 10^{+01}$	6.29×10^{-01}
0.200	3.41×10^{-17}	5.43×10^{-17}	9.60×10^{-17}	$-3.740 \times 10^{+01}$	5.19×10^{-01}
0.250	5.88×10^{-14}	7.56×10^{-14}	1.00×10^{-13}	$-3.019 \times 10^{+01}$	2.78×10^{-01}
0.300	9.32×10^{-12}	1.13×10^{-11}	1.38×10^{-11}	$-2.520 \times 10^{+01}$	1.96×10^{-01}
0.350	3.46×10^{-10}	4.08×10^{-10}	4.86×10^{-10}	$-2.162 \times 10^{+01}$	1.69×10^{-01}
0.400	5.11×10^{-09}	5.95×10^{-09}	6.98×10^{-09}	$-1.894 \times 10^{+01}$	1.56×10^{-01}
0.450	4.09×10^{-08}	4.72×10^{-08}	5.50×10^{-08}	$-1.686 \times 10^{+01}$	1.47×10^{-01}
0.500	2.13×10^{-07}	2.44×10^{-07}	2.82×10^{-07}	$-1.522 \times 10^{+01}$	1.41×10^{-01}
0.600	2.47×10^{-06}	2.79×10^{-06}	3.20×10^{-06}	$-1.278 \times 10^{+01}$	1.32×10^{-01}
0.700	1.39×10^{-05}	1.57×10^{-05}	1.78×10^{-05}	$-1.106 \times 10^{+01}$	1.25×10^{-01}
0.800	5.15×10^{-05}	5.77×10^{-05}	6.51×10^{-05}	$-9.758 \times 10^{+00}$	1.18×10^{-01}
0.900	1.48×10^{-04}	1.66×10^{-04}	1.88×10^{-04}	$-8.701 \times 10^{+00}$	1.19×10^{-01}
1.000	3.65×10^{-04}	4.11×10^{-04}	4.73×10^{-04}	$-7.788 \times 10^{+00}$	1.35×10^{-01}
1.250	2.33×10^{-03}	2.77×10^{-03}	3.43×10^{-03}	$-5.867 \times 10^{+00}$	2.02×10^{-01}
1.500	(1.45×10^{-02})	(1.79×10^{-02})	(2.21×10^{-02})	$(-4.024 \times 10^{+00})$	(2.12×10^{-01})
1.750	(7.64×10^{-02})	(9.45×10^{-02})	(1.17×10^{-01})	$(-2.360 \times 10^{+00})$	(2.12×10^{-01})
2.000	(3.00×10^{-01})	(3.70×10^{-01})	(4.58×10^{-01})	(-9.932×10^{-01})	(2.12×10^{-01})
2.500	$(2.55 \times 10^{+00})$	$(3.15 \times 10^{+00})$	$(3.89 \times 10^{+00})$	$(1.147 \times 10^{+00})$	(2.12×10^{-01})
3.000	$(1.24 \times 10^{+01})$	$(1.53 \times 10^{+01})$	$(1.89 \times 10^{+01})$	$(2.729 \times 10^{+00})$	(2.12×10^{-01})
3.500	$(4.18 \times 10^{+01})$	$(5.17 \times 10^{+01})$	$(6.39 \times 10^{+01})$	$(3.945 \times 10^{+00})$	(2.12×10^{-01})
4.000	$(1.10 \times 10^{+02})$	$(1.36 \times 10^{+02})$	$(1.68 \times 10^{+02})$	$(4.913 \times 10^{+00})$	(2.12×10^{-01})
5.000	$(4.71 \times 10^{+02})$	$(5.82 \times 10^{+02})$	$(7.19 \times 10^{+02})$	$(6.366 \times 10^{+00})$	(2.12×10^{-01})
6.000	$(1.33 \times 10^{+03})$	$(1.64 \times 10^{+03})$	$(2.03 \times 10^{+03})$	$(7.405 \times 10^{+00})$	(2.12×10^{-01})
7.000	$(2.91 \times 10^{+03})$	$(3.59 \times 10^{+03})$	$(4.44 \times 10^{+03})$	$(8.186 \times 10^{+00})$	(2.12×10^{-01})
8.000	$(5.35 \times 10^{+03})$	$(6.62 \times 10^{+03})$	$(8.18 \times 10^{+03})$	$(8.798 \times 10^{+00})$	(2.12×10^{-01})
9.000	$(8.68 \times 10^{+03})$	$(1.07 \times 10^{+04})$	$(1.33 \times 10^{+04})$	$(9.281 \times 10^{+00})$	(2.12×10^{-01})
10.000	$(1.30 \times 10^{+04})$	$(1.60 \times 10^{+04})$	$(1.98 \times 10^{+04})$	$(9.681 \times 10^{+00})$	(2.12×10^{-01})

TABLE VII. Monte Carlo reaction rates for the $^{22}Ne(\alpha, n)^{25}Mg$ reaction. Shown are the low, median, and high rates, corresponding to the 16th, 50th, and 84th percentiles of the Monte Carlo probability density distributions. Also shown are the parameters (μ and σ) of the log-normal approximation to the actual Monte Carlo probability density. See Ref. [22] for details. The rate values shown in parentheses indicate the temperatures ($T > T_{\text{match}} = 1.33$ GK) for which Hauser-Feshbach rates, normalized to experimental results, are adopted (see Sec. II C).

T (GK)	Low rate	Median rate	High rate	log-normal μ	log-normal σ
0.010	0.0	0.0	0.0	—	—
0.011	0.0	0.0	0.0	—	—
0.012	0.0	0.0	0.0	—	—
0.013	0.0	0.0	0.0	—	—
0.014	0.0	0.0	0.0	—	—
0.015	0.0	0.0	0.0	—	—
0.016	0.0	0.0	0.0	—	—
0.018	0.0	0.0	0.0	—	—
0.020	0.0	0.0	0.0	—	—
0.025	0.0	0.0	0.0	—	—
0.030	5.12×10^{-88}	5.08×10^{-87}	2.25×10^{-86}	$-1.991 \times 10^{+02}$	$1.90 \times 10^{+00}$
0.040	1.46×10^{-67}	1.49×10^{-66}	6.64×10^{-66}	$-1.519 \times 10^{+02}$	$1.94 \times 10^{+00}$
0.050	2.99×10^{-55}	3.05×10^{-54}	1.36×10^{-53}	$-1.236 \times 10^{+02}$	$1.95 \times 10^{+00}$
0.060	4.92×10^{-47}	4.87×10^{-46}	2.17×10^{-45}	$-1.047 \times 10^{+02}$	$1.92 \times 10^{+00}$
0.070	3.70×10^{-41}	3.48×10^{-40}	1.55×10^{-39}	$-9.117 \times 10^{+01}$	$1.84 \times 10^{+00}$
0.080	1.03×10^{-36}	8.44×10^{-36}	3.73×10^{-35}	$-8.101 \times 10^{+01}$	$1.74 \times 10^{+00}$
0.090	3.23×10^{-33}	2.19×10^{-32}	9.43×10^{-32}	$-7.309 \times 10^{+01}$	$1.62 \times 10^{+00}$
0.100	2.17×10^{-30}	1.20×10^{-29}	4.92×10^{-29}	$-6.673 \times 10^{+01}$	$1.50 \times 10^{+00}$
0.110	4.65×10^{-28}	2.12×10^{-27}	8.22×10^{-27}	$-6.151 \times 10^{+01}$	$1.39 \times 10^{+00}$
0.120	4.24×10^{-26}	1.62×10^{-25}	5.82×10^{-25}	$-5.714 \times 10^{+01}$	$1.29 \times 10^{+00}$
0.130	1.94×10^{-24}	6.61×10^{-24}	2.14×10^{-23}	$-5.342 \times 10^{+01}$	$1.19 \times 10^{+00}$
0.140	5.27×10^{-23}	1.64×10^{-22}	4.81×10^{-22}	$-5.020 \times 10^{+01}$	$1.08 \times 10^{+00}$
0.150	9.94×10^{-22}	2.74×10^{-21}	7.18×10^{-21}	$-4.737 \times 10^{+01}$	9.62×10^{-01}
0.160	1.43×10^{-20}	3.39×10^{-20}	7.89×10^{-20}	$-4.484 \times 10^{+01}$	8.29×10^{-01}
0.180	1.61×10^{-18}	2.74×10^{-18}	5.01×10^{-18}	$-4.040 \times 10^{+01}$	5.53×10^{-01}
0.200	9.14×10^{-17}	1.24×10^{-16}	1.79×10^{-16}	$-3.660 \times 10^{+01}$	3.43×10^{-01}
0.250	1.68×10^{-13}	2.06×10^{-13}	2.53×10^{-13}	$-2.921 \times 10^{+01}$	2.06×10^{-01}
0.300	2.74×10^{-11}	3.36×10^{-11}	4.15×10^{-11}	$-2.411 \times 10^{+01}$	2.06×10^{-01}
0.350	1.05×10^{-09}	1.29×10^{-09}	1.59×10^{-09}	$-2.046 \times 10^{+01}$	2.05×10^{-01}
0.400	1.64×10^{-08}	2.00×10^{-08}	2.45×10^{-08}	$-1.773 \times 10^{+01}$	1.99×10^{-01}
0.450	1.42×10^{-07}	1.71×10^{-07}	2.07×10^{-07}	$-1.558 \times 10^{+01}$	1.88×10^{-01}
0.500	8.51×10^{-07}	1.00×10^{-06}	1.19×10^{-06}	$-1.381 \times 10^{+01}$	1.68×10^{-01}
0.600	1.74×10^{-05}	1.92×10^{-05}	2.15×10^{-05}	$-1.085 \times 10^{+01}$	1.07×10^{-01}
0.700	2.36×10^{-04}	2.51×10^{-04}	2.69×10^{-04}	$-8.287 \times 10^{+00}$	6.70×10^{-02}
0.800	2.15×10^{-03}	2.27×10^{-03}	2.42×10^{-03}	$-6.084 \times 10^{+00}$	5.79×10^{-02}
0.900	1.36×10^{-02}	1.43×10^{-02}	1.51×10^{-02}	$-4.246 \times 10^{+00}$	5.33×10^{-02}
1.000	6.34×10^{-02}	6.64×10^{-02}	6.98×10^{-02}	$-2.711 \times 10^{+00}$	4.82×10^{-02}
1.250	$1.18 \times 10^{+00}$	$1.22 \times 10^{+00}$	$1.27 \times 10^{+00}$	1.998×10^{-01}	3.88×10^{-02}
1.500	$(1.09 \times 10^{+01})$	$(1.14 \times 10^{+01})$	$(1.18 \times 10^{+01})$	$(2.431 \times 10^{+00})$	(3.89×10^{-02})
1.750	$(6.79 \times 10^{+01})$	$(7.06 \times 10^{+01})$	$(7.34 \times 10^{+01})$	$(4.257 \times 10^{+00})$	(3.89×10^{-02})
2.000	$(2.92 \times 10^{+02})$	$(3.04 \times 10^{+02})$	$(3.16 \times 10^{+02})$	$(5.717 \times 10^{+00})$	(3.89×10^{-02})
2.500	$(2.74 \times 10^{+03})$	$(2.85 \times 10^{+03})$	$(2.96 \times 10^{+03})$	$(7.953 \times 10^{+00})$	(3.89×10^{-02})
3.000	$(1.41 \times 10^{+04})$	$(1.46 \times 10^{+04})$	$(1.52 \times 10^{+04})$	$(9.590 \times 10^{+00})$	(3.89×10^{-02})
3.500	$(4.96 \times 10^{+04})$	$(5.16 \times 10^{+04})$	$(5.37 \times 10^{+04})$	$(1.085 \times 10^{+01})$	(3.89×10^{-02})
4.000	$(1.36 \times 10^{+05})$	$(1.41 \times 10^{+05})$	$(1.47 \times 10^{+05})$	$(1.186 \times 10^{+01})$	(3.89×10^{-02})
5.000	$(6.10 \times 10^{+05})$	$(6.34 \times 10^{+05})$	$(6.59 \times 10^{+05})$	$(1.336 \times 10^{+01})$	(3.89×10^{-02})
6.000	$(1.80 \times 10^{+06})$	$(1.88 \times 10^{+06})$	$(1.95 \times 10^{+06})$	$(1.444 \times 10^{+01})$	(3.89×10^{-02})
7.000	$(4.07 \times 10^{+06})$	$(4.23 \times 10^{+06})$	$(4.40 \times 10^{+06})$	$(1.526 \times 10^{+01})$	(3.89×10^{-02})
8.000	$(7.70 \times 10^{+06})$	$(8.01 \times 10^{+06})$	$(8.32 \times 10^{+06})$	$(1.590 \times 10^{+01})$	(3.89×10^{-02})
9.000	$(1.28 \times 10^{+07})$	$(1.33 \times 10^{+07})$	$(1.39 \times 10^{+07})$	$(1.640 \times 10^{+01})$	(3.89×10^{-02})
10.000	$(1.97 \times 10^{+07})$	$(2.04 \times 10^{+07})$	$(2.12 \times 10^{+07})$	$(1.683 \times 10^{+01})$	(3.89×10^{-02})

(iii) high $^{22}Ne(\alpha, n)^{25}Mg$ rate and low $^{22}Ne(\alpha, \gamma)^{26}Mg$ rate. Although in reality the $^{22}Ne(\alpha, \gamma)^{26}Mg$ and $^{22}Ne(\alpha, n)^{25}Mg$ rates will be correlated, it is difficult to account for these correlations since the $^{22}Ne(\alpha, \gamma)^{26}Mg$ rate includes resonances

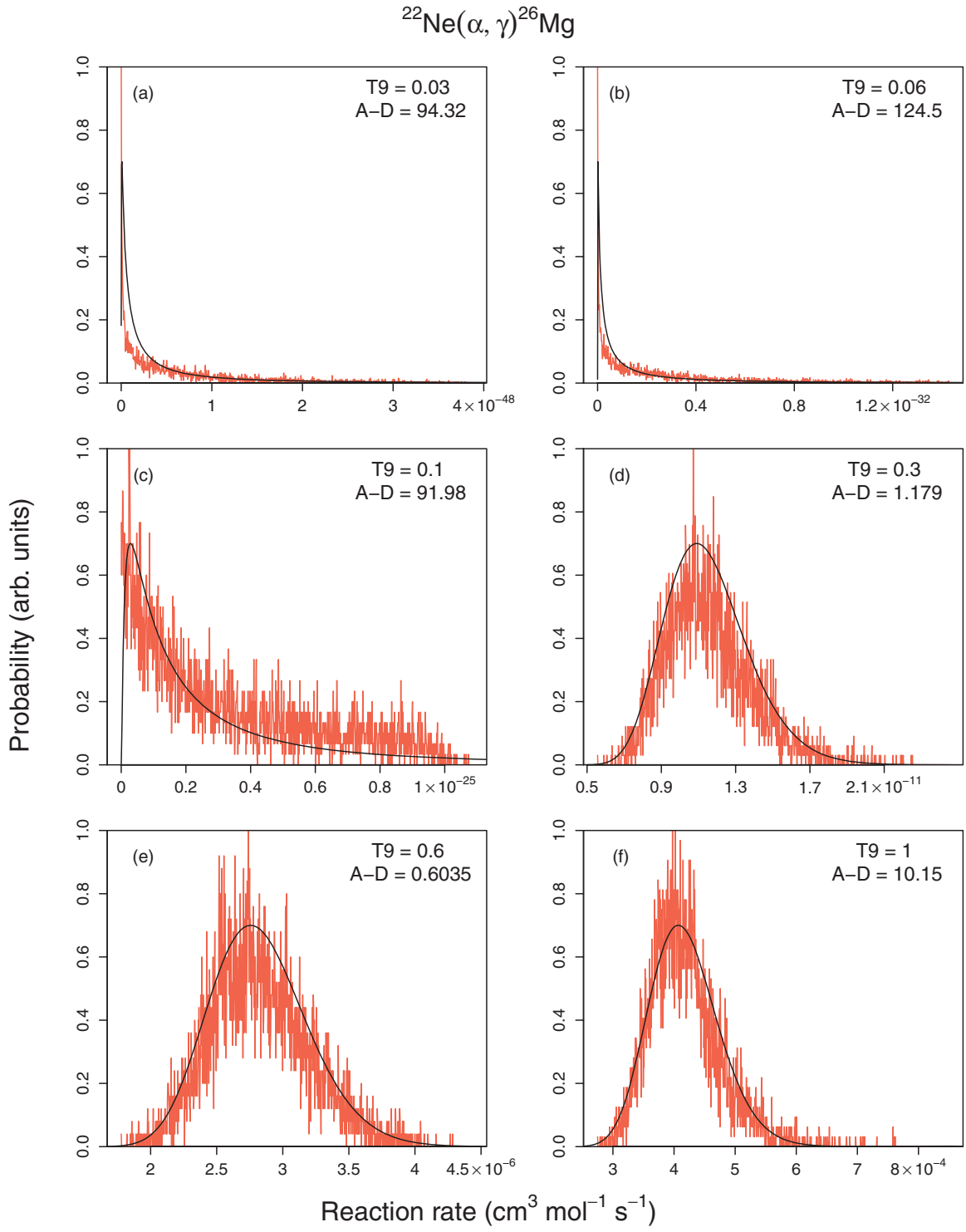

FIG. 2. (Color online) Reaction rate probability densities for the ^{22}Ne(α, γ)^{26}Mg reaction at various stellar temperatures. In each panel, the red histogram represents the Monte Carlo results, while the solid line shows the log-normal approximation. Note that the solid line is *not* a fit to the histogram but was calculated from the log-normal parameters μ and σ (Table VI), which in turn were determined from Eq. (12). It is apparent that the log-normal approximation to the reaction rates holds in the temperature range of the *s*-process (near 0.3 GK).

below the neutron threshold and since some ^{26}Mg levels contribute more to one reaction channel than the other. For these reasons, we have chosen in the present study to explore conservatively the impact of the largest reaction rate variations. These nucleosynthesis calculations are performed separately for massive stars and AGB stars.

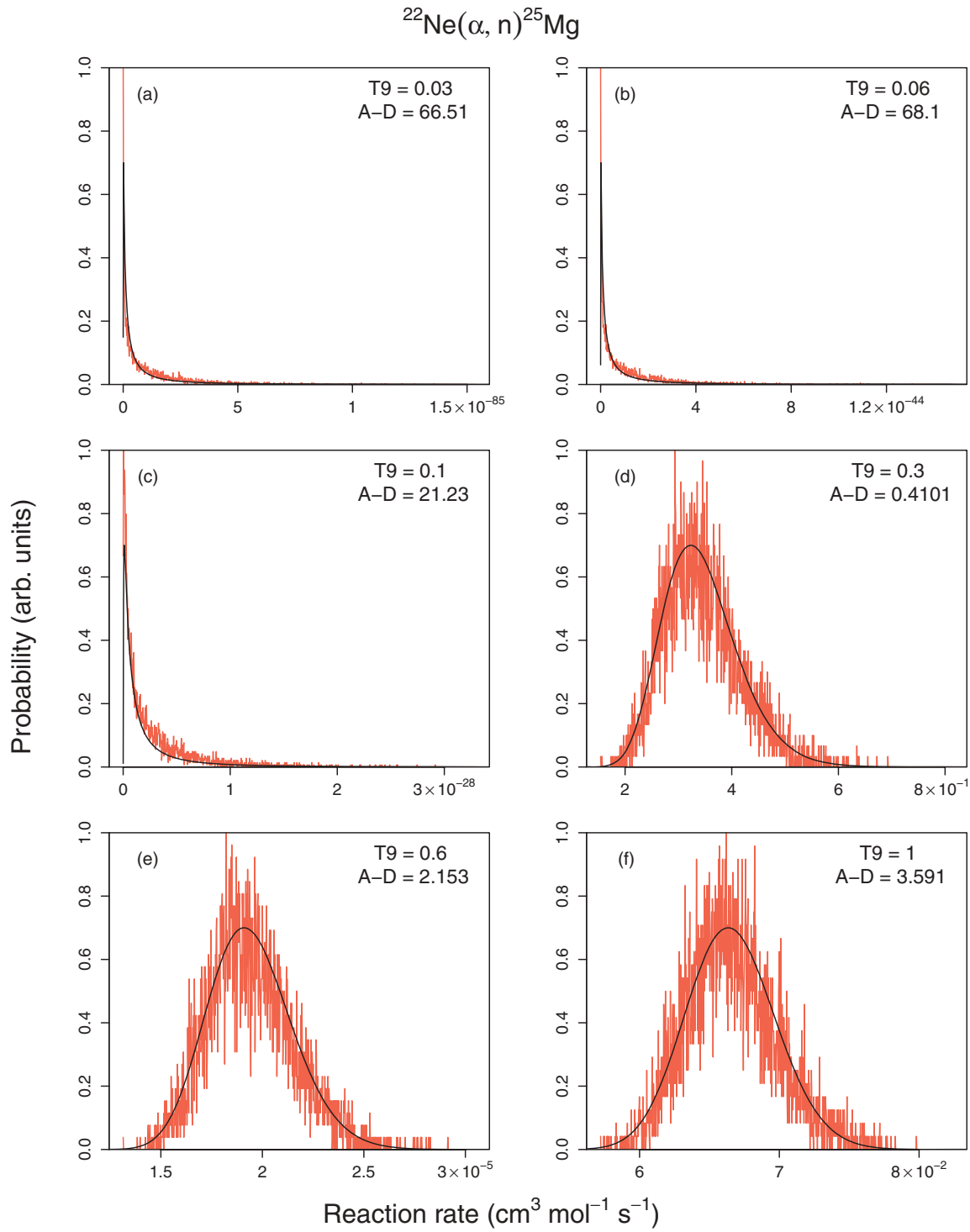

FIG. 3. (Color online) Reaction rate probability densities for the ^{22}Ne(α, n)^{25}Mg reaction. (See the caption to Fig. 2.)

1. Massive star models

A single-zone temperature-density profile has been used to study the effects of the $^{22}\mathrm{Ne}+\alpha$ reaction rates on nucleosynthesis during the core-helium-burning stage in massive stars. The temperature-density profile and initial abundances used in the present study are for a $25M_{\odot}$ star and have been used previously in Refs. [24,58]. The most abundant isotopes at the onset of helium burning are (in mass fractions, X): ^{4}He ($X_{\alpha} = 0.982$), ^{14}N ($X_{^{14}\mathrm{N}} = 0.0122$), ^{20}Ne ($X_{^{20}\mathrm{Ne}} = 0.0016$), and ^{60}Fe ($X_{^{60}\mathrm{Fe}} = 0.00117$). During most of the core-helium-burning phase, the temperature and density ($T \approx 100$–250 MK and $\rho \approx 1000$–2000 g/cm^3, respectively) are not high enough for the ^{22}Ne(α, n)^{25}Mg neutron source to produce a significant number of neutrons. However, toward the end of this phase

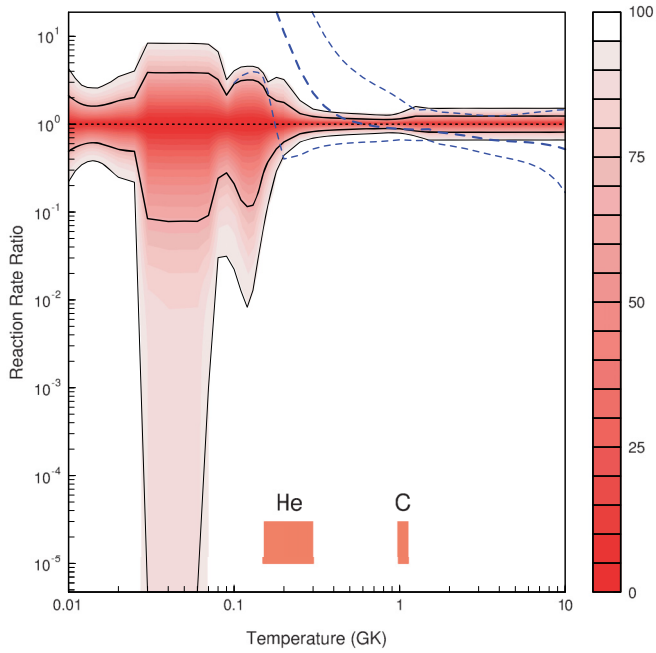

FIG. 4. (Color online) The uncertainty bands for the ^{22}Ne$(\alpha,\gamma)^{26}$Mg reaction. The uncertainties are the result of upper limit resonance contributions and of resonance strength uncertainties. The color densities represent the present reaction rate probability densities normalized to our recommended rate. The thick and thin black lines represent the 68% and 95% uncertainties, respectively. The dashed blue lines represent the literature rates from Ref. [18], with the thick and thin lines denoting the recommended rate and rate limits, respectively, normalized to our recommended rate. Values below unity (dotted line) indicate that the rates are lower than the present recommended rate. The relevant temperatures for helium- and carbon-shell burning have been added as red bars with the labels "He" and ",C" respectively.

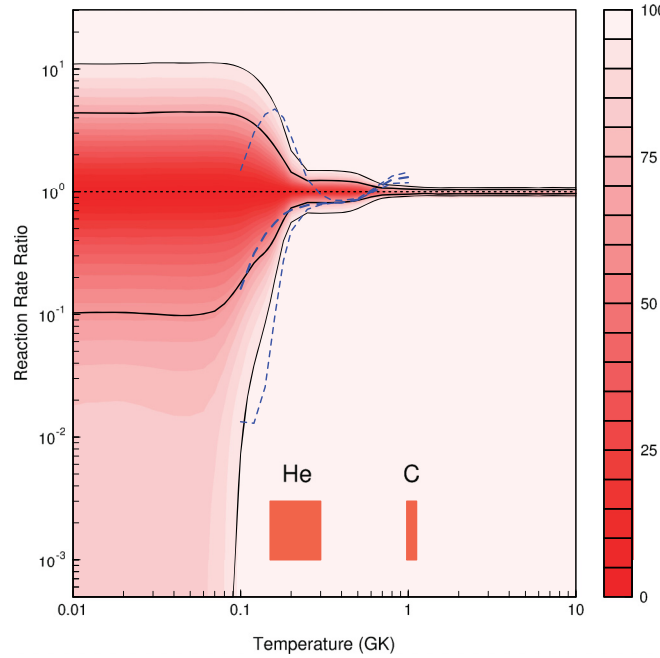

FIG. 5. (Color online) The probability densities for the ^{22}Ne$(\alpha,n)^{25}$Mg reaction in comparison to those presented by Ref. [19]. See caption of Fig. 4 for an explanation.

the temperatures become high enough for efficient neutron production. The exact time at which the ^{22}Ne$(\alpha,n)^{25}$Mg reaction starts to occur affects not only the number of neutrons produced during core helium burning but also the amount of ^{22}Ne remaining that can be processed later during the carbon-shell-burning phase. Although not studied here, the s-process is also expected to be active during carbon-shell burning.

The nucleosynthesis study was performed with a 583-nucleus s-process network that extends up to molybdenum. Reaction rates (other than the ^{22}Ne$+\alpha$ rates) were adopted from the starlib library [65]. The starlib library incorporates a compilation of recently evaluated experimental Monte Carlo reaction rates in tabular format on a grid of 60 temperatures from 1 MK to 10 GK. Tabulated are the temperature, the reaction rate, and the factor uncertainty, which is closely related to the log-normal parameter, σ, in Ref. [22].

2. AGB star models

The AGB nucleosynthesis tests are performed on a $5.5M_{\odot}$, $Z = 0.0001$ model star, detailed in Ref. [66]. This model was chosen because it experiences many thermal pulses (77 in total) during the AGB phase, where 69 of those He-shell instabilities reach peak temperatures of 0.30 GK or higher (with temperatures of 0.35 GK for 50 thermal pulses). One complication arises from disentangling the effects of the ^{22}Ne$+\alpha$ rates and those of proton-capture nucleosynthesis at the base of the convective envelope (hot bottom burning, HBB). In our model, the base of the envelope reaches peak temperatures of 98 MK, easily hot enough for activation of the NeNe and MgAl proton-burning chains. The main results were reductions in the envelope ^{24}Mg and ^{25}Mg abundances and increases in ^{26}Mg, ^{26}Al, and ^{27}Al. This means that the He intershell preceding a pulse contains a nonsolar Mg isotopic composition that is enriched in ^{26}Mg.

The postprocessing nucleosynthesis used for the AGB star models has previously been described in detail in, e.g., Ref. [66]. This code needs as input from the stellar evolution code variables such as temperature, density, and convective boundaries as a function of time and mass fraction. The code then traces the abundance changes as a function of mass and time using a nuclear network containing 172 species (from neutrons to sulfur, and then from iron to molybdenum) and assuming time-dependent diffusive mixing for all convective zones [67]. Although this network does not contain species of the main s-process above $A \approx 100$, their production is estimated by the inclusion of an extra isotope (the "g" particle, counting neutron captures beyond our network). The reaction rates used in the nuclear network are mostly taken from the JINA reaclib database [68], with the exception of the ^{22}Ne$+\alpha$ rates adopted from the present work. Some modifications were made to the JINA reaclib library including the removal of the ^{96}Zr decay rate (since this is an essentially stable isotope with a half-life of $t_{1/2} \geqslant 10^{19}$ yr) and the inclusion of the

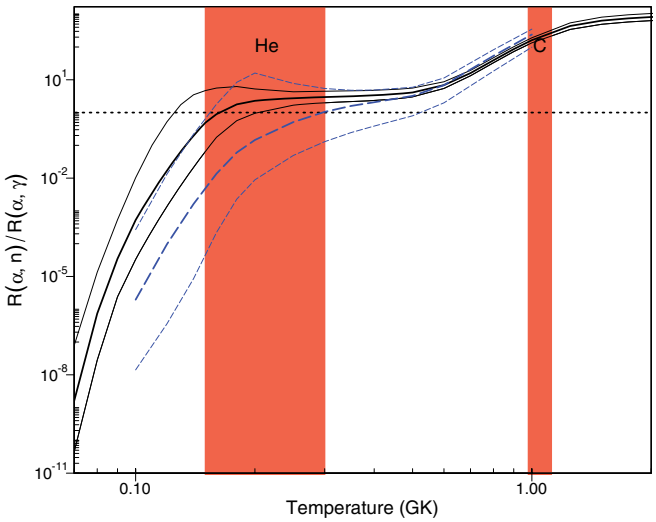

FIG. 6. (Color online) Uncertainty bands of the reaction rate *ratio*, $N_A\langle\sigma v\rangle_{(\alpha,n)}/N_A\langle\sigma v\rangle_{(\alpha,\gamma)}$. The solid (black) lines represent the present reaction rate ratio, while the dashed (blue) lines represent the ratio of rates from Ref. [19] for ^{22}Ne$(\alpha,n)^{25}$Mg and from Ref. [18] for ^{22}Ne$(\alpha,\gamma)^{26}$Mg. The recommended ratio (the center line in each set) was calculated by dividing the recommended ^{22}Ne$(\alpha,n)^{25}$Mg reaction rate by that of the ^{22}Ne$(\alpha,\gamma)^{26}$Mg reaction at each temperature. To obtain the uncertainty bands for the rate ratio, the high rate for ^{22}Ne$(\alpha,\gamma)^{26}$Mg was divided by the low rate for ^{22}Ne$(\alpha,n)^{25}$Mg, and vice versa. Values greater than unity indicate that more neutrons (and ^{25}Mg) are produced than γ rays (and ^{26}Mg) per α-particle capture. The temperatures relevant in helium- and carbon-shell burning are represented by red bars and are marked with "He" and "C," respectively.

ground and isomeric states in ^{85}Kr. This is done because 50% of the neutron flux from $n+^{84}$Kr proceeds to the ground state of ^{85}Kr ($t_{1/2} = 3934.4$ days) and the other 50% goes to the isomeric state ($\tau = 4.480$ h). The inclusion of both ^{85}Kr states is essential for Rb abundance predictions in AGB nucleosynthesis models (see the discussion in Refs. [8,69]).

B. Results

The effects of our new rates on the nucleosynthesis in comparison to using the results obtained in the literature are shown in Fig. 7. The improvements in abundance predictions for the two stellar environments are shown in Fig. 8. The most up-to-date previously published rates for the ^{22}Ne$(\alpha,\gamma)^{26}$Mg and ^{22}Ne$(\alpha,n)^{25}$Mg reactions are from Refs. [18] and [19], respectively. The effects are markedly different for the two s-process environments, and hence they will be discussed separately in the following.

1. Massive stars

The recommended ^{22}Ne$(\alpha,n)^{25}$Mg reaction rate has not changed significantly in the present analysis. Consequently, we do not expect the final ^{25}Mg abundance to change. The final ^{26}Mg abundance, on the other hand, changes significantly by roughly a factor of 3. The abundance changes in nuclei heavier

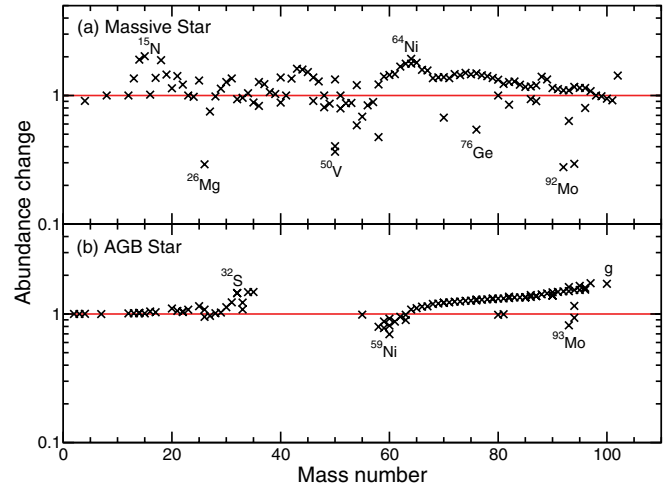

FIG. 7. (Color online) Ratio of final abundances resulting from the new recommended ^{22}Ne$(\alpha,\gamma)^{26}$Mg and ^{22}Ne$(\alpha,n)^{25}$Mg rates to those obtained from the old recommended rates. Points above unity (red line) represent a net increase in abundance. (a) At the end of core He burning in a $25M_\odot$ star, the most significant abundances affected by the new rates are those of ^{26}Mg and the p-nuclei ^{74}Se, ^{78}Kr, and ^{84}Sr. (b) For AGB stars, higher mass nuclei are produced in larger quantities, as evidenced by the "g" particle that monitors neutron captures above molybdenum.

than iron are smaller, with the largest abundance increases occurring near ^{64}Ni. The increased destruction of isotopes already present in the star is also apparent for the p-nuclides ^{74}Se, ^{78}Kr, ^{84}Sr, and ^{93}Nb. These results indicate that, with the reduced ^{22}Ne$(\alpha,\gamma)^{26}$Mg rate, more neutrons are produced per ^{22}Ne $+\,\alpha$ reaction. Rather than extending the reach of the weak s-process component (i.e., synthesis of more massive

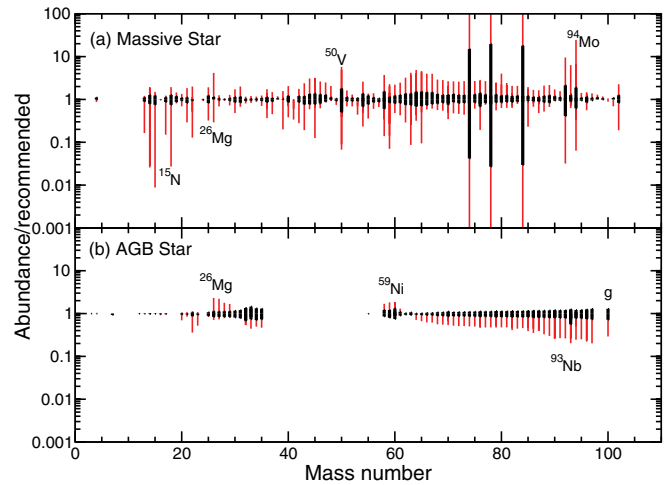

FIG. 8. (Color online) Comparison of abundance variations vs mass number arising from ^{22}Ne $+\,\alpha$ rate uncertainties presented in the literature (Ref. [18] for the ^{22}Ne$(\alpha,\gamma)^{26}$Mg reaction rate and Ref. [19] for the ^{22}Ne$(\alpha,n)^{25}$Mg reaction rate) and from the current ^{22}Ne $+\,\alpha$ rate uncertainties. Abundance changes based on the present and previous rate uncertainties are shown as thick black bars and thin red bars, respectively, for (a) massive stars and (b) AGB stars.

nuclei), this flux increase affects branchings in the s-process path close to the iron peak. A wider range of intermediate-mass nuclei are therefore produced. Figure 7 also illustrates that the $^{22}\mathrm{Ne}+\alpha$ rates affect not only the abundances of traditional s-process nuclides but also the abundances of nuclei below the iron peak that act as poisons. An example is ^{25}Mg, which produces ^{26}Mg through the $^{25}\mathrm{Mg}(n,\gamma)^{26}\mathrm{Mg}$ reaction. With a higher flux of available neutrons, this neutron poison reaction occurs more frequently, effectively lessening the impact of the increased neutron flux on s-process nucleosynthesis.

Uncertainties in s-process nucleosynthesis in massive stars arising from uncertainties in the $^{22}\mathrm{Ne}+\alpha$ reaction rates are shown in Fig. 8, where the thin (red) bars show uncertainties arising from the old rates, and thicker (black) bars show those from the new rates. In particular, large reductions are noticeable for ^{26}Mg, where the current yield uncertainty amounts to around 50%, in contrast to the previous factor of 5. Uncertainties in weak s-process nucleosynthesis have also undergone significant improvements, especially for species that can only be destroyed, but not created, by neutron captures. An example of this is the nucleus ^{58}Ni, whose yield uncertainty has been reduced from a factor of 5 to just 50%. It is important to note here that, although the Monte Carlo reaction rates do take into account systematic uncertainties, it is difficult to account for ambiguities in the data, for example, the open question of whether or not the $E_r^{\mathrm{lab}} = 830$ keV resonance is a doublet. Clearly, more measurements are needed.

2. AGB stars

Nucleosynthesis yields from our low-metallicity AGB star models show a very different pattern to those of the massive star study. For AGB stars, the effect on lighter elements is reduced in comparison to massive stars, with higher mass s-process elements revealing the largest changes. This weighting toward higher mass s-process elements is caused by our choice of using a low-metallicity model. At low metallicity, the neutron/Fe seed ratio is much higher, meaning that there is a higher production of higher atomic mass nuclei (e.g., see the discussion in Refs. [9,70]). Nuclei toward the upper end of our network are produced up to a factor of 2 more than before, with the "g" particle representing nuclei beyond our network, capturing over 70% more neutrons. In low-metallicity AGB stars, therefore, the $^{22}\mathrm{Ne}+\alpha$ reactions can be expected to produce more high-mass s-process elements, while leaving the low-mass s-process below $A \approx 80$ largely unaffected.

Uncertainties in s-process nucleosynthesis have been, as in massive stars, dramatically improved with our new rates. The previous abundance uncertainties were approximately a factor of 10, while the present uncertainties amount to less than a factor of 2. The present uncertainties in the rates affect the lower masses from $A \approx 25$ to $A \approx 35$ more than the s-process abundances. The ratio of ^{26}Mg and ^{25}Mg is still uncertain by approximately 20%, whereas the uncertainty was previously around 80% (but note that in Ref. [12] $^{26}\mathrm{Mg}/^{25}\mathrm{Mg}$ ratio uncertainties of 60% were found). Rubidium and zirconium isotopes have undergone yield uncertainty improvements by a factor of about 2. For the s-nuclide ^{96}Mo, the uncertainty has been reduced from a factor of 4 to a factor of 2 with our present results.

The new $^{22}\mathrm{Ne}+\alpha$ reaction rates presented here should also be tested with low-mass AGB star models ($M \leqslant 3M_{\odot}$). In lower mass AGB stars, while the $^{13}\mathrm{C}(\alpha,n)^{16}\mathrm{O}$ reaction is the main neutron source active between thermal pulses, activation of the $^{22}\mathrm{Ne}+\alpha$ reactions during a convective thermal pulse can have a significant effect on branchings in the s-process path.

VII. CONCLUSIONS

Both the $^{22}\mathrm{Ne}(\alpha,n)^{25}\mathrm{Mg}$ and the $^{22}\mathrm{Ne}(\alpha,\gamma)^{26}\mathrm{Mg}$ reactions influence the neutron flux available to the s-process in massive stars and AGB stars. Uncertainties in the rates, therefore, lead to large uncertainties in s-process nucleosynthesis. In this paper, we have estimated greatly improved $^{22}\mathrm{Ne}+\alpha$ reaction rates, based on newly available experimental information published since the works of Refs. [19] and [18] and by applying a sophisticated rate computational method [22]. Subsequently, we explored the astrophysical consequences for massive stars and for AGB stars.

In massive stars, simple one-zone models of core helium burning were utilized to determine the influence of the new rates on the weak component of the s-process. The most important result of our study is a significant reduction of nucleosynthesis uncertainties. The yield uncertainty has been reduced by between a factor of 5 and 10 across the s-process mass region considered here ($A < 100$). For example, the yields of key isotopes, ^{26}Mg and ^{70}Zn, have uncertainty reduction factors of about 5 and 10, respectively. When comparing abundances obtained from our new recommended rates with those derived from previous recommended rates, the final yield of ^{26}Mg is found to have been reduced by roughly a factor of 3, while s-process isotopes were affected only marginally. However, s-process nucleosynthesis is more concentrated around the iron peak when using the new reaction rates. This relative insensitivity to changes in neutron flux is partially caused by captures on the neutron poisons ^{12}C, ^{16}O, and ^{25}Mg, which are present in large quantities.

In our AGB star models, the final abundance uncertainties have also been improved significantly with the new rates, with reductions by up to an order of magnitude. The key rubidium and zirconium isotopes, for example, have undergone yield uncertainty improvements of roughly a factor of 2. We have also found that s-process nucleosynthesis is more active when including the new $^{22}\mathrm{Ne}+\alpha$ reaction rates. While only small changes are found in the low-mass s-process path ($A < 80$), at higher masses production increases by up to a factor of 2. This is especially evident by counting the number of captures at the end of our network, yielding an increase of over 70%. Further calculations should be performed to study the effect of our new rates on lower mass AGB stars, while paying special attention to their effects on branchings in the s-process path.

The Monte Carlo method used in the present study to calculate the $^{22}\mathrm{Ne}+\alpha$ reaction rates has the distinct advantage of calculating the uncertainties in a robust and statistical meaningful manner. Although our rates include some of the

systematic uncertainties in the nuclear data, there are still open questions regarding the resonance properties that could affect the rates. Clearly, the remaining ambiguities in the nuclear data for the $^{22}\mathrm{Ne}+\alpha$ reaction rates need to be resolved. The discrepancies discussed here, by Koehler [60], and by Karakas *et al*. [12], make it difficult to assign some ^{26}Mg levels to $^{22}\mathrm{Ne}+\alpha$ resonances. Furthermore, the $E_r^{\mathrm{lab}} = 831$ keV resonance should be remeasured with high precision. More information should also be gathered on the structure of ^{26}Mg levels near the α-particle and neutron thresholds. Indirect methods such as particle transfer measurements are useful here, since the Coulomb barrier inhibits direct measurements.

ACKNOWLEDGMENTS

This work was supported in part by the US Department of Energy under Grant No. DE-FG02-97ER41041 and the National Science Foundation under Award No. AST-1008355. This work was also partially supported by the Spanish grant AYA2010-15685 and the ESF EUROCORES Program EuroGENESIS through MICINN Grant No. EUI2009-04167. AIK thanks Maria Lugaro and Joelene Buntain for help with setting up the nucleosynthesis code that reads in tables. AIK is grateful for the support of the NCI National Facility at the ANU. RL would like to thank James deBoer for the in-depth discussions about properties of ^{26}Mg levels and the $^{22}\mathrm{Ne}+\alpha$ reactions.

[1] C. Sneden, J. J. Cowan, and R. Gallino, Annu. Rev. Astron. Astrophys. **46**, 241 (2008).
[2] F. Käppeler, R. Gallino, S. Bisterzo, and W. Aoki, Rev. Mod. Phys. **83**, 157 (2011).
[3] H. Habing and H. Olofsson, *Asymptotic Giant Branch Stars* (Springer, New York, 2004).
[4] F. Herwig, Annu. Rev. Astron. Astrophys. **43**, 435 (2005).
[5] M. Pignatari, R. Gallino, F. Käppeler, and M. Wiescher, Nucl. Phys. A **758**, 541 (2005).
[6] D. A. García-Hernández, P. García-Lario, B. Plez, F. D'Antona, A. Manchado, and J. M. Trigo-Rodríguez, Science **314**, 1751 (2006).
[7] M. Lugaro and M. van Raai, J. Phys. G **35**, 014007 (2008).
[8] D. A. García-Hernández, A. Manchado, D. L. Lambert, B. Plez, P. García-Lario, F. D'Antona, M. Lugaro, A. I. Karakas, and M. A. van Raai, Astrophys. J. Lett. **705**, L31 (2009).
[9] A. I. Karakas, D. A. García-Hernández, and M. Lugaro, Astrophys. J. **751**, 8 (2012).
[10] D. Yong, F. Grundahl, D. L. Lambert, P. E. Nissen, and M. D. Shetrone, Astron. Astrophys. **402**, 985 (2003).
[11] D. Yong, D. L. Lambert, and I. I. Ivans, Astrophys. J. **599**, 1357 (2003).
[12] A. I. Karakas, M. A. Lugaro, M. Wiescher, J. Görres, and C. Ugalde, Astrophys. J. **643**, 471 (2006).
[13] L. The, M. F. El Eid, and B. S. Meyer, Astrophys. J. **655**, 1058 (2007).
[14] S. E. Woosley and A. Heger, Phys. Rep. **442**, 269 (2007).
[15] M. Pignatari, R. Gallino, M. Heil, M. Wiescher, F. Kppeler, F. Herwig, and S. Bisterzo, Astrophys. J. **710**, 1557 (2010).
[16] A. L. Piro and L. Bildsten, Astrophys. J. **673**, 1009 (2008).
[17] F. X. Timmes, E. F. Brown, and J. W. Truran, Astrophys. J. Lett. **590**, L83 (2003).
[18] C. Angulo *et al*., Nucl. Phys. A **656**, 3 (1999).
[19] M. Jaeger, R. Kunz, A. Mayer, J. W. Hammer, G. Staudt, K. L. Kratz, and B. Pfeiffer, Phys. Rev. Lett. **87**, 202501 (2001).
[20] C. Iliadis, R. Longland, A. E. Champagne, A. Coc, and R. Fitzgerald, Nucl. Phys. A **841**, 31 (2010).
[21] R. J. deBoer, M. Wiescher, J. Görres, R. Longland, C. Iliadis, G. Rusev, and A. P. Tonchev, Phys. Rev. C **82**, 025802 (2010).
[22] R. Longland, C. Iliadis, A. E. Champagne, J. R. Newton, C. Ugalde, A. Coc, and R. Fitzgerald, Nucl. Phys. A **841**, 1 (2010).
[23] G. Audi, A. H. Wapstra, and C. Thibault, Nucl. Phys. A **729**, 337 (2003).
[24] C. Iliadis, *Nuclear Physics of Stars* (Wiley–VCH, New York, 2007).
[25] C. Iliadis, Nucl. Phys. A **618**, 166 (1997).
[26] A. Belhout *et al*., Nucl. Phys. A **793**, 178 (2007).
[27] A. M. Lane and R. G. Thomas, Rev. Mod. Phys. **30**, 257 (1958).
[28] N. Keeley, K. W. Kemper, and D. T. Khoa, Nucl. Phys. A **726**, 159 (2003).
[29] W. J. Thompson and C. Iliadis, Nucl. Phys. A **647**, 259 (1999).
[30] R. Longland, Ph.D. thesis, University of North Carolina at Chapel Hill, 2010.
[31] C. Iliadis, J. M. D'Auria, S. Starrfield, W. J. Thompson, and M. Wiescher, Astrophys. J. Suppl. Ser. **134**, 151 (2001).
[32] C. E. Porter and R. G. Thomas, Phys. Rev. **104**, 483 (1956).
[33] H. A. Weidenmüller and G. E. Mitchell, Rev. Mod. Phys. **81**, 539 (2009).
[34] P. E. Koehler, F. Bečvář, M. Krtička, J. A. Harvey, and K. H. Guber, Phys. Rev. Lett. **105**, 072502 (2010).
[35] P. E. Koehler, Phys. Rev. C **84**, 034312 (2011).
[36] J. M. Drake, E. G. Bilpuch, G. E. Mitchell, and J. F. Shriner Jr., Phys. Rev. C **49**, 411 (1994).
[37] T. W. Anderson and D. A. Darling, J. Am. Stat. Assoc. **49**, 765 (1954).
[38] J. R. Newton, R. Longland, and C. Iliadis, Phys. Rev. C **78**, 025805 (2008).
[39] T. Rauscher and F.-K. Thielemann, At. Data Nucl. Data Tables **75**, 1 (2000).
[40] K. Wolke, H. W. Becker, C. Rolfs, U. Schröder, H. P. Trautvetter, V. Harms, K. L. Kratz, J. W. Hammer, M. Wiescher, and A. Wöhr, Z. Phys. A **334**, 491 (1989).
[41] V. Harms, K.-L. Kratz, and M. Wiescher, Phys. Rev. C **43**, 2849 (1991).
[42] H. W. Drotleff, A. Denker, J. W. Hammer, H. Knee, S. Küchler, D. Streit, C. Rolfs, and H. P. Trautvetter, Z. Phys. A **338**, 367 (1991).
[43] H. W. Drotleff, A. Denker, H. Knee, M. Soine, G. Wolf, J. W. Hammer, U. Greife, C. Rolfs, and H. P. Trautvetter, Astrophys. J. **414**, 735 (1993).
[44] U. Giesen *et al*., Nucl. Phys. A **561**, 95 (1993).
[45] J. W. Hammer, in *Proceedings of the International Workshop XXVI on Gross Properties of Nuclei and Nuclear Excitations*, edited by M. Buballa, W. Nörenberg, J. Wambach, and A. Wirzba (GSI-Darmstadt, Germany, 1998), p. 370.
[46] U. N. Singh, H. I. Liou, J. Rainwater, G. Hacken, and J. B. Garg, Phys. Rev. C **10**, 2150 (1974).

[47] H. Weigmann, R. L. Macklin, and J. A. Harvey, Phys. Rev. C **14**, 1328 (1976).
[48] L. W. Fagg, Rev. Mod. Phys. **47**, 683 (1975).
[49] C. E. Moss, Nucl. Phys. A **269**, 429 (1976).
[50] A. Tamii *et al*., Nucl. Phys. A **788**, 53 (2007).
[51] U. E. P. Berg, K. Ackermann, K. Bangert, C. Blsing, W. Naatz, R. Stock, K. Wienhard, M. K. Brussel, T. E. Chapuran, and B. H. Wildenthal, Phys. Lett. B **140**, 191 (1984).
[52] G. M. Crawley, C. Djalali, N. Marty, M. Morlet, A. Willis, N. Anantaraman, B. A. Brown, and A. Galonsky, Phys. Rev. C **39**, 311 (1989).
[53] R. Schwengner, A. Wagner, Y. Fujita, G. Rusev, M. Erhard, D. De Frenne, E. Grosse, A. R. Junghans, K. Kosev, and K. D. Schilling, Phys. Rev. C **79**, 037303 (2009).
[54] F. Glatz *et al*., Z. Phys. A **324**, 187 (1986).
[55] M. Yasue *et al*., Phys. Rev. C **42**, 1279 (1990).
[56] C. Ugalde *et al*., Phys. Rev. C **76**, 025802 (2007).
[57] B. L. Berman, R. L. van Hemert, and C. D. Bowman, Phys. Rev. Lett. **23**, 386 (1969).
[58] L. The, M. F. El Eid, and B. S. Meyer, Astrophys. J. **533**, 998 (2000).
[59] R. Longland, C. Iliadis, G. Rusev, A. P. Tonchev, R. J. deBoer, J. Görres, and M. Wiescher, Phys. Rev. C **80**, 055803 (2009).
[60] P. E. Koehler, Phys. Rev. C **66**, 055805 (2002).
[61] F. E. Wietfeldt and G. L. Greene, Rev. Mod. Phys. **83**, 1173 (2011).
[62] P. Descouvemont, A. Adahchour, C. Angulo, A. Coc, and E. Vangioni-Flam, At. Data Nucl. Data Tables **88**, 203 (2004).
[63] T. A. Walkiewicz, S. Raman, E. T. Jurney, J. W. Starner, and J. E. Lynn, Phys. Rev. C **45**, 1597 (1992).
[64] P. M. Endt, Nucl. Phys. A **521**, 1 (1990).
[65] C. Iliadis, A. Champagne, A. Chieffi, and M. Limongi, Astrophys. J. Suppl. Ser. **193**, 16 (2011).
[66] A. I. Karakas, Mon. Not. R. Astron. Soc. **403**, 1413 (2010).
[67] R. C. Cannon, Mon. Not. R. Astron. Soc. **263**, 817 (1993).
[68] R. H. Cyburt *et al*., Astrophys. J. Suppl. Ser. **189**, 240 (2010).
[69] M. Lugaro and A. Chieffi, in *Astronomy with Radioactivities, Lecture Notes in Physics*, Vol. 812, edited by R. Diehl, D. H. Hartmann, and N. Prantzos (Springer, New York, 2011), pp. 83–152.
[70] M. Busso, R. Gallino, D. L. Lambert, C. Travaglio, and V. V. Smith, Astrophys. J. **557**, 802 (2001).